Doctoral Thesis

Thesis Title

Author:

Ana Andres-Arroyo

Supervisor:

Dr. First Last

A thesis submitted in fulfilment of the requirements for the degree of Doctor of Philosophy

School of Physics, Faculty of Science

November 2018

Dedicated to someone.

"Fancy Quote"

Author

Abstract

School of Physics, Faculty of Science, UNSW Australia

Doctor of Philosophy

Thesis Title

by Ana Andres-Arroyo

Write your abstract here .

Acknowledgements

The acknowledgements and the people to thank go here, don't forget to include your project advisor…

Contents

List of Figures

Abbreviations

2D Two-**D**imensional

3D Three-**D**imensional

Physical Constants

Speed of Light	c	$=$	$2.997\ 924\ 58 \times 10^{8}$ $\mathrm{ms}^{-\mathrm{S}}$ (exact)
Constant Name	Symbol	$=$	Constant Value (with units)

Symbols

f	focal length	mm or cm
H	heating	K/W
I	intensity	a.u.
k	trap stiffness	pN/μm/mW
n	refractive index	—
P	power	mW
T	temperature	°C or K

ε	permittivity	???
κ	trap stiffness	pN/μm/mW
λ	wavelength	nm
μ	permeability	???
σ	cross section	???
θ	tilt angle	degrees or radians

Chapter 1

Introduction

1.1 Section title

Always put labelthesection after each section so the page headers work.

This is a test.

1.2 Compiling instructions

1. make the main file the masted document: options -¿ make current file masted document
2. Quick build from anywhere (because it quick builds from the master document
3. BibTex from the chapter file (disable the master document option for this and do it from "normal mode")
4. Quick build 3 times (from the master document): 1 for the text, 2 for the references and labels, 3 for the bibliography backreferencing.

1.3 References

Chapter 2

Using Fourier transform phase for the measurement of radial velocity

---

This chapter introduces a new method for measuring radial velocities. Specifically, it uses the Fourier transform of a line profile (or cross-correlation profile) to distinguish between the effects of a bulk shift in that profile (i.e. a radial velocity shift of the profile), as opposed to a change in the line profile shape which can produce an apparent radial velocity shift. We examine the impact on the Fourier transformed components of a line profile of both bulk line shifts, and line profile deformations, with the aim of developing tools to distinguish between these two cases.

There are a lot of simulations involved in this chapter. To make things clear, the following diagram shows a quick roadmap of the tests made with the newly proposed technique – Fourier transform phase analysis, and how the simulations are organized in the chapter, for future reference.

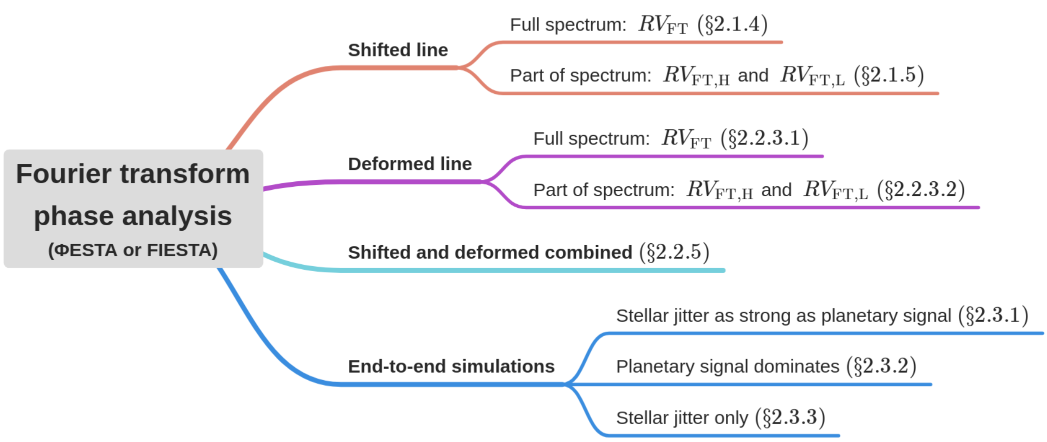

Fig. 2.1: Roadmap of Fourier transform phase analysis on simulated data.

2.1 Phase analysis of Fourier transform for the measurement of line shift

The translation of a function (in our case a spectral line profile) can be examined in both its original real space, and in its Fourier transformed space. Because Fourier transform is often used to handle time domain data, a shift in real space can be variously described as either time shifting or translation. In this chapter we will use "time shifting", "translation" and "velocity shifting" interchangeably to refer to a shift of a function in real space. We will refer to Fourier transformed functions as being in the "frequency domain" regardless of whether they have actual dimensions of 1/time, 1/length or 1/velocity.

2.1.1 Translation property of Fourier transform

Let us consider a function $h(x)$ as a signal $f(x)$ delayed (or shifted) by an amount x_0:

$$h(x) = f(x - x_0). \tag{2.1}$$

In the frequency domain, we will then have

$$\hat{h}(\xi) = e^{-2\pi i x_0 \xi} \hat{f}(\xi), \tag{2.2}$$

where the circumflex denotes the Fourier transform of a function, i.e.

$$\hat{f}(\xi) = \int_{-\infty}^{\infty} f(x) e^{-2\pi i x \xi} dx. \tag{2.3}$$

E.q. 2.2 means that while the power spectrum remains unchanged for shifted signals, i.e. $\mid \hat{h}(\xi) \mid^2 = \mid \hat{f}(\xi) \mid^2$, the phases $\phi(\xi)$, defined as the argument of the Fourier representation $\hat{f}(\xi)$: $\mathrm{Arz}(\hat{f}(\xi))$, have changed because of the additional term $e^{-2\pi i x_0 \xi}$. The extra phases $\Delta\phi(\xi)$ added are:

$$\Delta\phi(\xi) = -2\pi x_0 \xi. \tag{2.4}$$

2.1.2 Intuitive explanation

An intuitive, but equally quantitative way, to see how E.q.2.4 holds is as follows. The Fourier transform decomposes the function $f(x)$ into a frequency representation $\hat{f}(\xi)$, accompanied by the orthogonal basis $e^{2\pi ix\xi}$, as in the form of inverse Fourier transform:

$$f(x) = \int_{-\infty}^{\infty} \hat{f}(\xi)e^{2\pi ix\xi}d\xi. \tag{2.5}$$

Shifting $f(x)$ by x_0 is equivalent to shifting *all* the orthogonal basis functions by x_0, which then become $e^{2\pi i(x-x_0)\xi} = e^{2\pi ix\xi}.e^{-2\pi ix_0\xi}$. This is how the additional term $e^{-2\pi ix_0\xi}$ in Eq. 2.2 arises – it quantifies the phase difference for a shifted function.

An even more intuitive but less quantitative way to envision the relation between a shift of the signal and a phase difference is to imagine any real continuous function is a sum of sines and cosines. Changing the phase angle in the sines and cosines results in shifts in the function.

The power spectrum of such a shifted function remains the same because shifting the signal as a whole doesn't add or remove any frequency components.

2.1.3 Practical Use

From Eq. 2.4, we see that the phase shift $\Delta\phi(\xi)$ is proportional to the frequency ξ with a constant gradient or slope

$$\frac{\mathrm{d}(\Delta\phi)}{\mathrm{d}\xi} = -2\pi x_0 \tag{2.6}$$

where Δ is used to refer to the phase difference between a shifted line profile and an unshifted (referenced) line profile, while the derivative refers to the response of $\Delta\phi(\xi)$ to ξ. $\Delta\phi(\xi)$ is measured as the change in phases $\mathrm{Arz}(\hat{h}(\xi)) - \mathrm{Arz}(\hat{f}(\xi))$. Then a linear regression model can be fit to a plot of $\Delta\phi(\xi)$ versus ξ (Fig. 2.2) to enable measurement of the bulk shift between two line profiles x_0.

By analogy with the definition of power spectrum, we describe $\phi(\xi)$ as the **phase spectrum** and hence $\Delta\phi(\xi)$ as the **differential phase spectrum**. In this approach, an analysis of the phase shift in the frequency domain of the Fourier components of a line profile will provide a means of measuring a bulk line shift in real space. We therefore name our method **FourIEr *phase* SpecTrum Analysis** ($\mathit{\Phi}$ESTA or FIESTA).

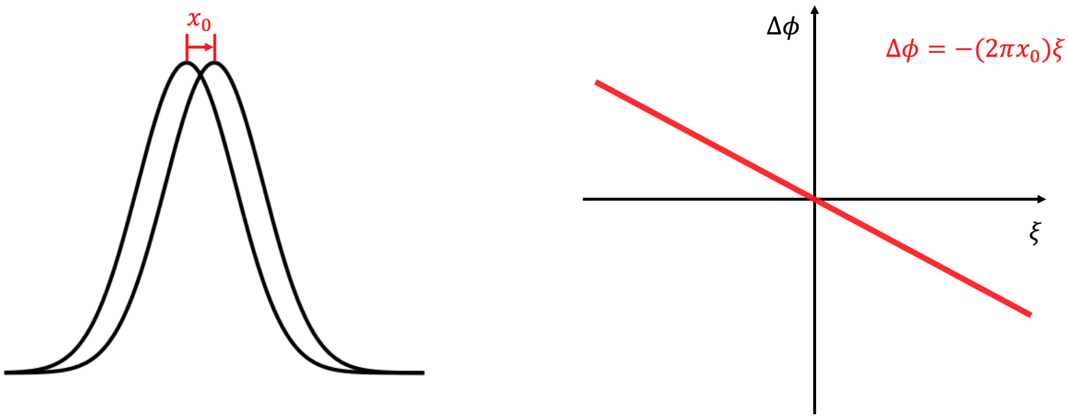

Fig. 2.2: The left panel shows a signal (or a spectral line profile in the following context) shifted by an amount x_0. The right panel is the differential phase spectral density diagram (i.e. differential phase spectrum). The model shows the phase difference between two shifted signals $\Delta\phi(\xi)$ and the frequency ξ are linearly correlated. Its slope $-2\pi x_0$ contains information of the amount of signal shift in time domain.

2.1.4 Initial tests to obtain $RV_{\mathbf{FT}}$

We performed an initial test to determine that we can correctly recover known shifts of a line profile using $\mathit{\Phi}$ESTA. We generated a spectral line profile based on the cross-correlation function of observed HARPS spectra with the software SOAP 2.0 [1]. This was replicated 100 times, with a very small amount of noise (equivalent to a S/N = 10,000) injected in each of the line profiles. These profiles were then subjected to radial velocity shifts evenly spaced between 0 and 10 m/s (Fig. 2.3).

The Fourier transform of these 100 spectral line profiles divides the information into two parts: (1) the power spectra (Fig. 2.4a) and (2) the phase spectra (shown in Fig. 2.4b as the differential phase spectra – the difference relative to the phase spectrum of the unshifted line profile rather than its own derivative). We see that most information is concentrated towards the centre of the power spectrum (i.e. the lower frequency range), and as expected, the differential phase spectra are mostly linear, consistent with the theory demonstrated in Fig. 2.2. Deviations from linearity come from the noise that we injected, which will be discussed later.

The slope of each differential phase spectrum indicates the shift of each line profile relative to the unshifted one. For a linear regression fitting, each frequency sample on the differential phase spectrum is weighted by the amplitude of the power, meaning the lower frequencies receive more weights. We calculate the radial velocity shift for each

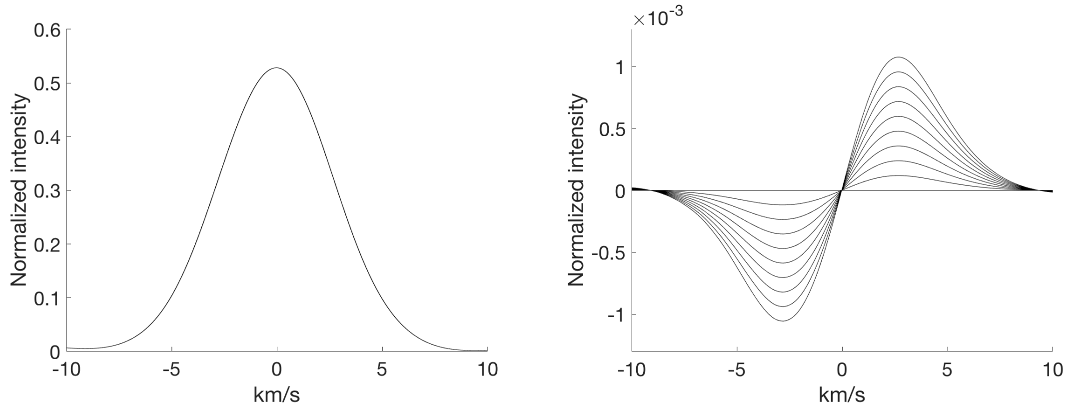

(a) Line profile (stacked) **(b)** Differential line profile

Fig. 2.3: (a) the shifted line profiles plotted on top of each other, showing that the 0-10 m/s shifts are very small compared to the line profile width. (b) the shifted line profiles with the unshifted line profile subtracted from each. Note that for the sake of clarity, the differential line profiles are plotted noise-free and only 10 out of 100 profiles are displayed.

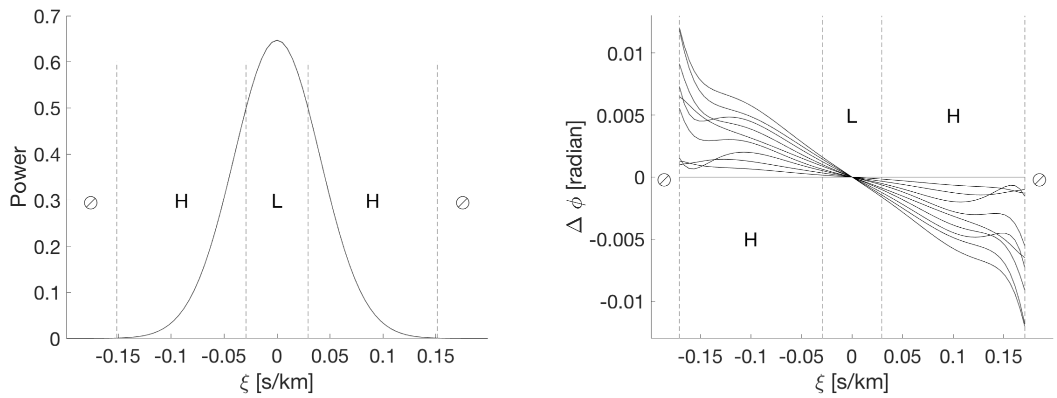

(a) Power spectrum (stacked) **(b)** Differential phase spectrum

Fig. 2.4: The Fourier transform of these shifted line profile divides the information in each into (a) their power spectra and (b) their phase spectra (here plotted differential compared to that of the unshifted profile). A line shift in the time domain produces an unchanged power spectrum in the frequency domain. It does, however, produce phase shifts which we see as linear trends in the differential phase spectra as a function of frequency. Only 10 out of 100 differential phase spectra are displayed. The differential phase spectrum can be sub-divided into higher frequency range (H) and lower frequency range (L). The ∅ region contains little power and frequency information and thus not used. We derive RV_{FT} from the full spectrum (except ∅), $RV_{\mathrm{FT,H}}$ from the higher frequency range and $RV_{\mathrm{FT,L}}$ from the lower frequency range.

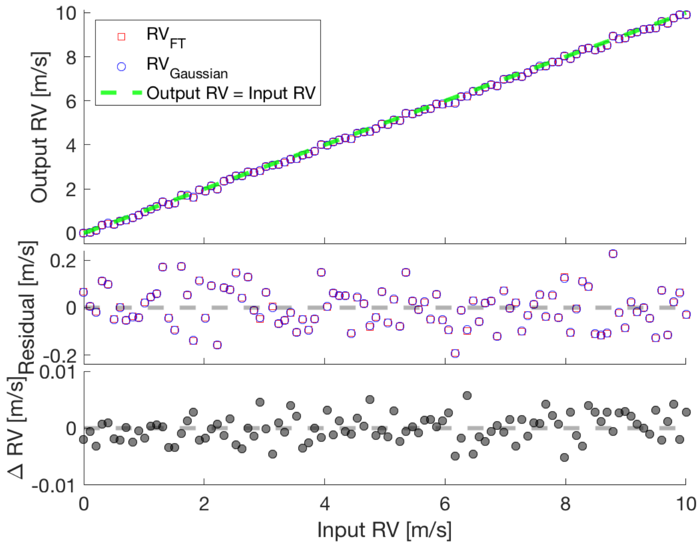

Fig. 2.5: Radial velocity recovery of line shifts with both methods: Fourier transform and Gaussian fit. Top: RV_{FT} and RV_{Gaussian} plotted against the input radial velocity shifts. Middle: residuals as RV_{FT} and RV_{Gaussian} subtracted by the input radial velocity shifts. Bottom: ΔRV defined as the difference between RV_{FT} and RV_{Gaussian}, showing the highly consistency between each other. Note that axes scales are different across the subplots; errorbars are estimated to be the size of scatter 0.08 m/s but are not plotted for clarity.

shifted line profile using two methods: (1) ΦESTA to determine RV_{FT}; (2) traditional measurement of the line centroid by fitting a Gaussian function to each line profile that delivers RV_{Gaussian}.

We then compare both RV_{FT} and RV_{Gaussian} with the known input line shift. Fig. 2.5 reveals the expected 1:1 correlation between the input radial velocity shift and the output – the line of best fit of a linear regression model presents a slope of 0.996 ± 0.006 with 95% confidence bounds for both RV_{FT} and RV_{Gaussian}. The standard deviation of the residuals are both $\sigma_{\mathrm{FT}} = \sigma_{\mathrm{Gaussian}} = 0.08$ m/s, identical up to two decimal places, indicating the expected radial velocities are consistently obtained by both methods. In fact, the almost overlapping residuals in Fig. 2.5 middle panel means that the two methods are so coherently different from the input radial velocity (by small amounts) that this scatter must come from the photon noise intrinsic to the simulated line profiles rather than the methods themselves.

CGT: How do these comare which what you'd expect from the S/N and the intrinsic line width (should say at some int what the intrinsic line width is.

2.1.5 Further tests to obtain $RV_{\mathbf{FT,H}}$ and $RV_{\mathbf{FT,L}}$

Let's recall the justification of measuring a line shift in its Fourier space – the shifting of a line (or a function), when viewed as shifting the sum of its Fourier basis functions (or any other basis functions), has equally the same amount of shift on every basis function, which can be measured as a phase shift in the Fourier phase spectrum. That is to say, utilising only part of the phase spectrum will also return the correct shift of a line profile, although it utilises less information. The motivation of this will be discussed in §2.2 when we look at line profile deformations.

We divide the whole frequency range available into two parts (Fig. 2.4) – a lower frequency range (i.e. apply a low-pass filter) and a higher frequency range (i.e. apply a high-pass filter). The dividing frequency ξ_{HL} can be chosen arbitrarily for the time being, for example, such that both the lower and higher frequency ranges take up half of the power spectrum $P(\xi)$:

$$\int_{\xi_L=0}^{\xi_{HL}} P(\xi)d\xi = \int_{\xi_{HL}}^{\xi_H} P(\xi)d\xi. \tag{2.7}$$

We assume here that the integration of the power spectrum measures the amount of "information" in the original line profile, so that we would put equal trust on the radial velocities obtained from the lower and higher frequencies (namely $RV_{\mathrm{FT,L}}$ and $RV_{\mathrm{FT,H}}$, or $RV_{\mathrm{FT,H/L}}$ for both). In addition, a cut-off frequency ξ_H is applied to the upper boundary of the high-pass filter (so is $-\xi_H$ on the negative part; but since it can be easily proved that the phase spectrum $\phi(\xi)$ of any function $f(x)$ is antisymmetric, i.e. $\phi(\xi) = -\phi(-\xi)$, therefore the differential phase spectrum $\Delta\phi(\xi)$ is also antisymmetric and we can simply focus on the non-negative part of the spectrum). Frequencies higher than ξ_H hardly contributes to the shape of the line profile as the power $P(\xi)$ converges to zero and thus not used. The cut-off frequency should be chosen large enough so that the frequency range to be used extracts the most information from the power spectrum and phase spectrum, but not as far up as going beyond the noise level. Empirically, it is safe to choose ξ_H where $P(\xi)$ drops to 0.01% of $\max\{P(\xi)\}$ for a high S/N = 10,000, as in our simulation. Lower S/N observations should be applied with a smaller ξ_H accordingly.

We presented in Fig. 2.5 an accurate recovery of the radial velocity shifts given by RV_{FT}, for which the full range of frequencies were used; For exactly the same set of data but sub-divided into two frequency ranges, we plot $RV_{\mathrm{FT,H/L}}$ against the input radial

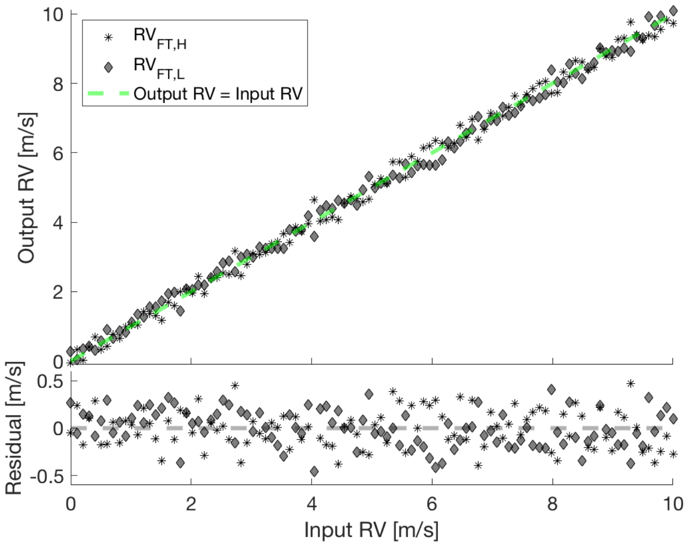

Fig. 2.6: Radial velocity recovery of line shifts with low-pass and high-pass filters. Errorbars are estimated to be around 0.2 m/s but not plotted for clarity.

velocities (Fig. 2.6), which still delivers a good 1:1 relation. The line of best fit presents a slope of 1.003 ± 0.010 for $RV_{\mathrm{FT,H}}$ and 0.991 ± 0.011 for $RV_{\mathrm{FT,L}}$ respectively, with 95% confidence bounds. The scatter of the residuals are $\sigma_{\mathrm{FT,H}} = 0.21$ m/s and $\sigma_{\mathrm{FT,L}} = 0.19$ m/s. First, we note that $\sigma_{\mathrm{FT,H/L}} > \sigma_{\mathrm{FT}}$ (=0.08 m/s), this is because both $RV_{\mathrm{FT,H}}$ and $RV_{\mathrm{FT,L}}$ are only derived from nearly half of the total "information" in the Fourier space. Second, we note that $\sigma_{\mathrm{FT,H}}$ and $\sigma_{\mathrm{FT,L}}$ only differ by a small amount, offering similar performance in recovering the radial velocity shifts, and this is because they are derived from roughly equal amount of "information".

2.1.6 Cut-off frequency

We mentioned in §2.1.4 that deviation from linearity in the differential phase spectrum may arise from the photon noise injected in the simulated line profiles, and we also introduced a cut-off frequency ξ_H in §2.1.5 to avoid dealing with frequencies higher than ξ_H. The motivation of these becomes clear on the frequency representation $\hat{f}(\xi)$ of a line profile in a complex plane (a.k.a. the Argand plane; Fig. 2.7).

We see a scattered plot because the frequencies ξ are discretely sampled. $\hat{f}(\xi)$ of noise-free and S/N = 10,000 are plotted for the same sampling of frequencies. The argument of $\hat{f}(\xi)$ returns the phase angle and the square of its absolute value (or modulus) returns the power. $\hat{f}(\xi)$ at larger power (i.e. those far from the origin as viewed in

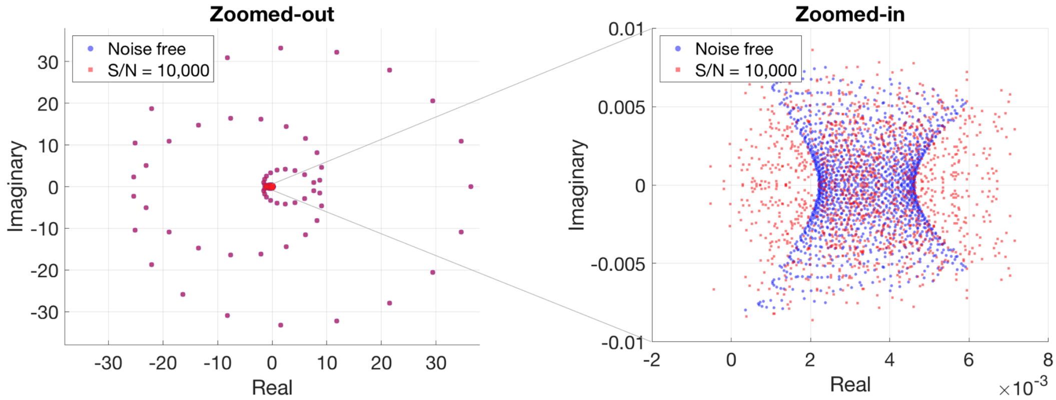

Fig. 2.7: The frequency representation $\hat{f}(\xi)$ of a line profile in a complex plane. The right panel is a zoom-in of the left near the origin. For the same sampling of frequencies, $\hat{f}(\xi)$ on the complex plane is less defined or more scattered in the presence of noise, making the measurement of the phase angle with a small amplitude far less reliable than measured without noise. This motivates us to come up with a cut-off frequency to relinquish $\hat{f}(\xi)$ higher than the threshold frequency, which is equivalent to abandoning amplitudes smaller than a threshold.

Fig. 2.7 left) is barely affected in the presence of noise; $\hat{f}(\xi)$ at lower power (i.e. those distributed in the vicinity of the origin as viewed in Fig. 2.7 right) are more affected by noise, as a slight displacement of $\hat{f}(\xi)$ in the complex plane means a considerable change in the phase angle. As a result, at S/N = 10,000, the distribution of $\hat{f}(\xi)$ in the zoomed-in complex plane is more scattered than a noise-free scenario, and the phase angle measurement is not as reliable as for $\hat{f}(\xi)$ with larger powers. This justifies using the Fourier transform spectral power as a weight, and introducing a cut-off frequency for shift measurements.

Another potential reason to introduce the cut-off frequency is the periodicity of the basis functions in a Fourier transform. The basis functions $e^{-2\pi i x_0 \xi}$ repeat themselves at the periods of $1/\xi$, making measuring the shift in the time domain (velocity domain for line profiles) larger than the order of $1/\xi$ degenerate (i.e. the shifts of $x_0 + k/\xi$ for $k \in \mathbb{Z}$ become indistinguishable). Nevertheless for cut-off frequency $\xi \sim 0.15$ s/km, such a shift needs to be more than $1/\xi \sim 6.7$ km/s to fail the measurement, while the radial velocities induced by planets are usually at m/s amplitudes and will not be a concern.

2.1.7 Conclusion

In this section, we have introduced a new method for measuring radial velocities – Fourier phase spectrum analysis (a.k.a ΦESTA or FIESTA). We tested this method on shifting a simulated line profile. It concludes that the newly proposed technique ΦESTA is able to measure a radial velocity shift at similarly high precision as fitting a line centroid by a Gaussian profile, and thus provides an alternative to the traditional means of obtaining the radial velocities.

In a broader context, this method will be applicable to measuring shifts of any pattern, and can also be extended to higher dimensions. In this thesis, we primarily focus on its use to measure radial velocity shifts in spectral line profiles.

2.2 Using the Fourier transform to probe line deformation

In § 2.1, we showed that *Φ*ESTA correctly measures the actual line profile shifts due to a bulk motion of the emitting star. In this section, we test whether this method is robust against spurious apparent radial velocity shifts produced by changes in the line profile shape.

2.2.1 Theory

For a line profile shifted by a small amount x_0, the same shift x_0 applies to *all* of its basis functions. Where a line profile is changed or deformed (as opposed to simply shifted), x_0 becomes frequency dependent. That is to say, basis functions at different frequencies would be shifted by different amounts to produce shape changes (e.g. skewness, kurtosis and higher order terms) in the line profile. Therefore we modify the translation property of Fourier transform by rewriting x_0 as $x_0(\xi)$ in Eq. 2.4:

$$\Delta\phi(\xi) = -2\pi x_0(\xi)\xi. \tag{2.8}$$

$x_0(\xi)$ contains all the information of how much a line is deformed (as well as shifted). In other words, $x_0(\xi)$ can parametrize the line deformation. In principle, we could derive $x_0(\xi)$ from the expression above to further seek to understand which frequency modes are related to stellar variability, as distinct from frequency modes responding to a bulk shift of a line profile. We opt for a simplistic approach instead – use an *averaged* shift $\overline{x_0(\xi)}$ to describe an overall shift of various frequency modes and rewrite Eq. 2.8 as

$$\Delta\phi(\xi) = -2\pi \overline{x_0(\xi)}\xi \tag{2.9}$$

where $\overline{x_0(\xi)}$ is treated as a constant for the range of frequencies of interest.

We may interpret E.q. 2.9 in two ways: (1) within a narrow frequency range, $x_0(\xi)$ is approximately a constant (hence labelled as $\overline{x_0(\xi)}$) and so the shift is proportional to the local gradient of the differential phase spectrum; (2) for a wide range of continuous frequencies, $\overline{x_0(\xi)}$ can be regarded as an effective line shift, and then we can study such shifts in the lower frequency range versus the higher frequency range the same way we dealt with a pure line shift in §2.1.

2.2.2 SOAP simulations

In § 2.1, we used the SOAP simulator to generate a line profile that resembles the HARPS observation to study a line shift in the Fourier space. In this section, we instead use SOAP 2.0 to study line deformations arising from starspots.

We injected three spots with different longitudes, latitudes and sizes (parameters were arbitrarily chosen and specified in Table 2.1) to model an emitting star. The spectral line profile is therefore deformed in the presence of spots. Such intrinsic line variabilities produce apparent radial velocities shifts (a.k.a. jitter) as a star rotates (also as spots themselves evolve with time, but such a feature is not automatically implemented in the SOAP simulator and we do not include this feature). The jitter amplitude depends on, but not limited to, the sizes and the positions of starspots; the three spots that we use present an amplitude of roughly 2 m/s. The same spot configuration is used in all simulations throughout the chapter.

We generated 100 cross-correlation functions for the resulting deformed line profiles evenly sampled throughout one rotation period of the star (Fig. 2.8). A very small amount of noise (equivalent to a S/N = 10,000) was also added into the line profiles in the simulation.

	Longitude	Latitude	Size in disk area percentage
Spot 1	174°	-14°	0.18%
Spot 2	288°	74°	0.40%
Spot 3	51°	52°	0.50%

Table 2.1: Spot configurations

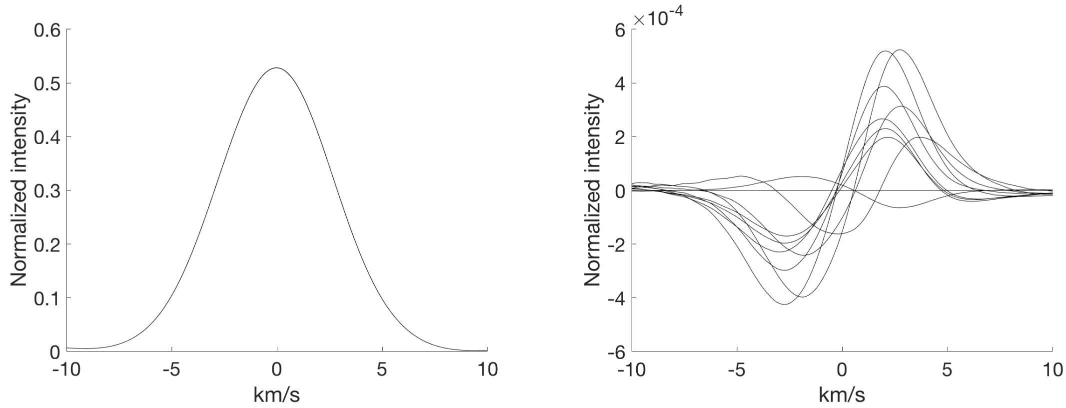

(a) Line profile (stacked) **(b)** Differential line profile

Fig. 2.8: Deformed line profile. For the sake of clarity, the differential line profiles are plotted noise-free and only 10 out of 100 profiles are presented.

2.2.3 Fourier phase spectrum analysis

2.2.3.1 $RV_{\mathbf{FT}}$

We took the same approach as previously (§ 2.1) to obtain the power spectrum and the differential phase spectrum (Fig. 2.9) and measured radial velocities RV_{FT} for the full range of frequencies. It is immediately apparent that a line deformation contributes to a skewed differential phase spectrum. As mentioned above, the shift $x_0(\xi)$ becomes frequency dependent, and is proportional to the local gradient of the differential phase spectrum.

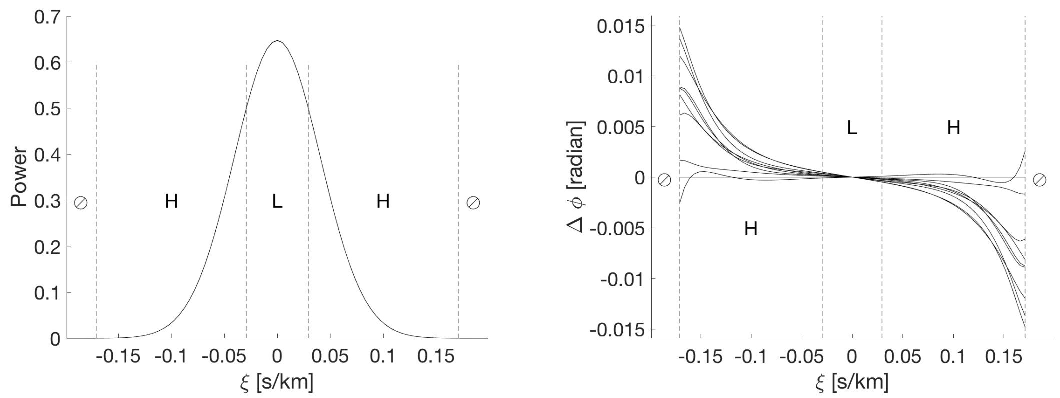

(a) Power spectrum (stacked) **(b)** Differential phase spectrum

Fig. 2.9: Fourier transform of deformed line profiles. Only 10 out of 100 differential phase spectra are presented.

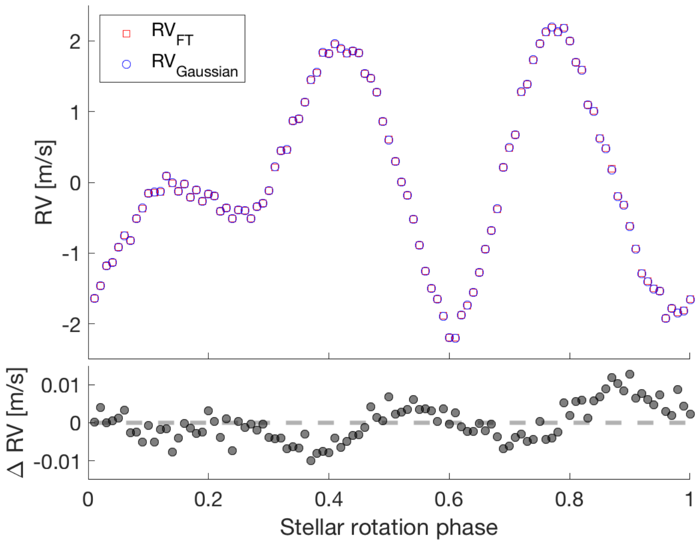

Fig. 2.10: Apparent RV of deformed line profiles calculated with both *ΦESTA* and Gaussian fit to the line profile. Both results are also highly consistent with each other. $\Delta RV = RV_{\mathrm{FT}} - RV_{\mathrm{Gaussian}}$.

For deformed line profiles, the traditionally measured radial velocities would be solely the apparent radial velocities due to deformed line profiles (a.k.a. jitter). Both velocities RV_{FT} and RV_{Gaussian} are plotted against rotation phase (Fig. 2.10). If we take $\sigma_{\mathrm{FT}} = \sigma_{\mathrm{Gaussian}} = 0.08$ m/s to be the intrinsic photon noise level corresponding to S/N = 10,000 as measured in § 2.1.4, and assume RV_{FT} and RV_{Gaussian} are independent measurements, the difference between RV_{FT} and RV_{Gaussian} would have an uncertainty of $\sqrt{\sigma^2_{\mathrm{FT}} + \sigma^2_{\mathrm{Gaussian}}} \approx 0.11$ m/s. Fig. 2.10 presents $| \Delta RV | = | RV_{\mathrm{FT}} - RV_{\mathrm{Gaussian}} | < 0.01$ m/s. Therefore, we can see that RV_{FT} and RV_{Gaussian} are indistinguishably consistent in the measurement of the apparent radial velocities of a deformed line profile. There is, however, a very small amount of bias between these two methods, as seen in the ΔRV trend. Increasing the cut-off frequency wisely can mitigate such bias.

2.2.3.2 $RV_{\mathrm{FT,H}}$ and $RV_{\mathrm{FT,L}}$

Although an intrinsic line deformation (in the absence of any velocity shift in the host star) usually mimics a radial velocity shift, we note the shape differences in the differential phase spectrum between an actual line shift (Fig. 2.4b) and a line deformation (Fig. 2.9b) – the latter presents slightly flatter features in lower frequencies and becomes more skewed towards higher frequencies. Such differences provide key information for differentiating the two situations.

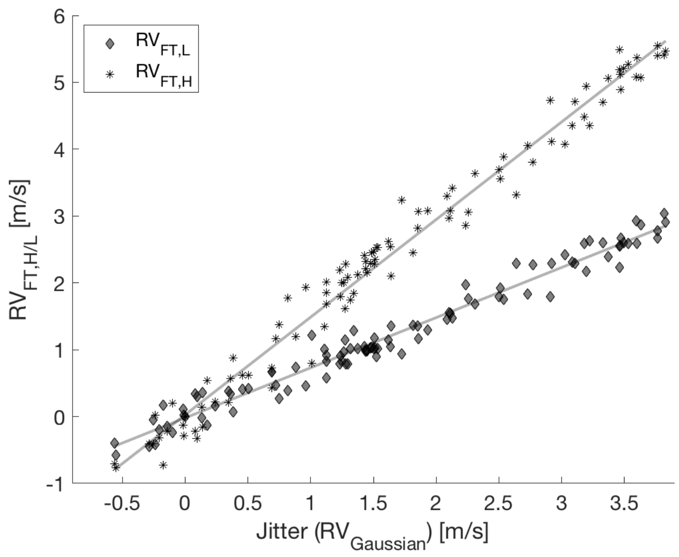

Fig. 2.11: Applying the low-pass and high-pass filters, the Fourier transform $RV_{\mathrm{FT,L}}$ and $RV_{\mathrm{FT,H}}$ are linearly correlated with the jitter (RV_{Gaussian}).

According to §2.2.1 where we introduced $\overline{x_0(\xi)}$ – an averaged shift for a particular frequency range – we compute the equivalent radial velocity shift for each of the lower and higher frequency ranges. We present our results by plotting the obtained $RV_{\mathrm{FT,H/L}}$ against the jitter (line centroid fitted by a Gaussian profile) in Fig. 2.11. The $RV_{\mathrm{FT,H}}$ and $RV_{\mathrm{FT,L}}$ are both linearly correlated with the jitter though with different slopes. Fitting with a linear regression model, it comes with a slope $k_{\mathrm{H}} = 1.491 \pm 0.053$ ($\pm 3.5\%$) for $RV_{\mathrm{FT,H}}$, meaning an apparent radial velocity shift of 1 m/s due to line deformation is detected as a 1.491 ± 0.053 m/s shift on average using *this* high-pass filter; whereas the slope for applying a low-pass filter is $k_{\mathrm{L}} = 0.750 \pm 0.027$ ($\pm 3.6\%$), not as "responsive" as $RV_{\mathrm{FT,H}}$ to the line profile deformation. It's also worth (and interesting) noting that the combined effect of these two filters would have resulted in RV_{FT}, a consistent measurement of the radial velocity as with the fitting a line centroid as previously showed.

We can investigate how well this correlation behaves for each filter by scaling the measured $RV_{\mathrm{FT,L}}$ and $RV_{\mathrm{FT,H}}$ by their corresponding factors $1/k_{\mathrm{L}}$ and $1/k_{\mathrm{H}}$ respectively, and compare them with the jitter (RV_{Gaussian}), presented in Fig. 2.12. The standard deviations for the residuals are $\sigma_{\mathrm{FT,H}} \approx 0.18$ m/s and $\sigma_{\mathrm{FT,L}} \approx 0.22$ m/s respectively, offering similar performance.

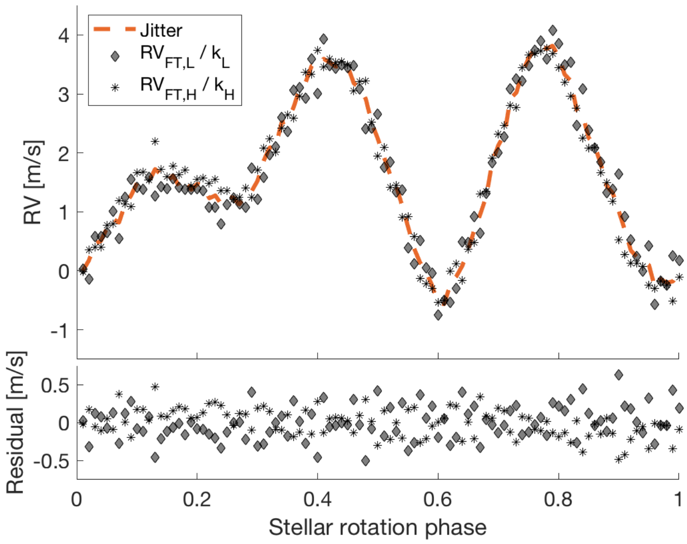

Fig. 2.12: Scaling the low-pass and high-pass Fourier transformed radial velocities to match the input jitter.

2.2.4 Jitter model

We have shown in § 2.1 that the following measurable quantities demonstrate essentially the same response to pure line shifts: RV_{FT}, $RV_{\mathrm{FT,H}}$, $RV_{\mathrm{FT,L}}$ and RV_{Gaussian}. We have also shown in § 2.2 that both $RV_{\mathrm{FT,H}}$ and $RV_{\mathrm{FT,L}}$ are linearly correlated with the jitter, and $RV_{\mathrm{FT,H}}$ is more responsive ($k_{\mathrm{H}} > 1$) than $RV_{\mathrm{FT,L}}$ ($k_{\mathrm{L}} < 1$).

We can therefore write the following measurable quantities – RV_{Gaussian} (or RV_{FT}), $RV_{\mathrm{FT,L}}$ and $RV_{\mathrm{FT,H}}$ – in the from of three additive terms: (1) a bulk shift in the star (which we hereafter assume to be due to a planet or planets as the superposition of Keplerian orbit(s)), (2) variability in the stellar line profile (hereafter lumped under the general name "jitter"), and (3) a constant radial velocity offset term chosen so as to be absorbed into the previous two terms.

$$RV_{\mathrm{Gaussian}} = RV_{\mathrm{planet}} + RV_{\mathrm{jitter}} \tag{2.10}$$

$$RV_{\mathrm{FT,L}} = RV_{\mathrm{planet}} + k_L \cdot RV_{\mathrm{jitter}} \tag{2.11}$$

$$RV_{\mathrm{FT,H}} = RV_{\mathrm{planet}} + k_H \cdot RV_{\mathrm{jitter}}. \tag{2.12}$$

Subtracting these equations to remove RV_{planet}, we reduce to two independent equations

$$RV_{\text{Gaussian}} - RV_{\text{FT,L}} = (1 - k_L) \cdot RV_{\text{jitter}} \tag{2.13}$$

$$RV_{\text{FT,H}} - RV_{\text{Gaussian}} = (k_H - 1) \cdot RV_{\text{jitter}} \tag{2.14}$$

Rearranging yields two expressions for the jitter model

$$RV_{\text{jitter}} = \frac{RV_{\text{Gaussian}} - RV_{\text{FT,L}}}{1 - k_L} \tag{2.15}$$

$$RV_{\text{jitter}} = \frac{RV_{\text{FT,H}} - RV_{\text{Gaussian}}}{k_H - 1} \tag{2.16}$$

where RV_{Gaussian}, $RV_{\text{FT,L}}$ and $RV_{\text{FT,H}}$ are direct measurements, whereas k_L and k_H are unknowns. We could determine k_L and k_H in the previous simulations only because we knew there were no radial velocities, other than jitter, in the system. These two expressions for the jitter model will be frequently used throughout the rest of the chapter. We therefore simplify $(RV_{\text{Gaussian}} - RV_{\text{FT,L}})$ as ΔRV_{L} and $(RV_{\text{FT,H}} - RV_{\text{Gaussian}})$ as ΔRV_{H} and call them the jitter matrices. Dividing the two equations above further cancels RV_{jitter} to give

$$\frac{\Delta RV_{\text{H}}}{\Delta RV_{\text{L}}} = \frac{k_H - 1}{1 - k_L} \triangleq k_{H/L}. \tag{2.17}$$

This means $(1 - k_H)/(1 - k_L)$ can now be obtained by fitting a linear regression model for ΔRV_{H} against ΔRV_{L}. With this, we rewrite the jitter model in a unified form – the weighted sum of the two jitter expressions from Eq. 2.15 and Eq. 2.16:

$$\begin{aligned} RV_{\text{jitter}} &= w_1 \frac{\Delta RV_{\text{L}}}{1 - k_L} + w_2 \frac{\Delta RV_{\text{H}}}{k_H - 1} \\ &= \frac{1}{1 - k_L} \left(w_1 \Delta RV_{\text{L}} + w_2 \frac{\Delta RV_{\text{H}}}{\frac{k_H - 1}{1 - k_L}} \right) \\ &= \alpha \left(w_1 \Delta RV_{\text{L}} + w_2 \frac{\Delta RV_{\text{H}}}{k_{H/L}} \right) \end{aligned} \tag{2.18}$$

in which the weights satisfy $w_1 + w_2 = 1$ and $1/(1 - k_L)$ is replaced by the scaling factor α.

An obvious check is to examine the correlation between ΔRV_{H} and ΔRV_{L} (Eq. 2.17) before going ahead creating the jitter model (Eq. 2.15 and Eq. 2.16). As our jitter model is solely based on the empirically assumed linear correlations between $RV_{\text{FT,H}}$, $RV_{\text{FT,L}}$ and RV_{jitter}, if either of these correlations fails, this can be detected by plotting ΔRV_{H} against ΔRV_{L}.

2.2.5 Testing the recovery of jitter

To begin with, we introduce a technique that smooths over noise in the observed signals – **weighted moving average** modulated by a Gaussian kernel. For N data points (e.g. radial velocities) v_i with an uncertainty σ_i observed at t_i ($i = 1, 2, ...N$), we define the contribution (i.e. weight) of a data point ($t_i, v_i \pm \sigma_i$) towards the chosen position t as the multiplication of two factors: (1) the weight of the data point itself, inversely proportional to the uncertainty squared: $W_i = 1/\sigma_i^2$ and (2) a stationary kernel that describes the correlation between data, depending on their distance $\mid t - t_i \mid$ and a time-scale of correlation τ: $K_i(t) = e^{-\frac{(t-t_i)^2}{2\tau^2}}$. With this, the evaluation of a data point $v(t)$ can be drawn by the weighted average of all observed data ($t_i, v_i \pm \sigma_i$), with the weight

$$\mathbf{W}_i(t) = W_i \cdot K_i(t) = \frac{1}{\sigma_i^2} e^{-\frac{(t-t_i)^2}{2\tau^2}} \tag{2.19}$$

respectively and then normalised by the sum of weights, so that

$$v(t) = \frac{\sum_{i=1}^{N} \left[v_i * \mathbf{W}_i(t) \right]}{\sum_{i=1}^{N} \mathbf{W}_i(t)} \tag{2.20}$$

To perform tests of the recovery of artificially generated jitter using Eq. 2.18, we doubled the amount of line profiles in the form of cross-correlation functions (i.e. simulated over a time equivalent to two stellar rotations), and each line profile is further shifted by an amount RV_{planet} with an amplitude of the Keplerian orbit $A_{\text{planet}} = 2$ m/s (although in principle the RV_{planet} configuration shouldn't affect the jitter model because the term was cancelled out when we derived the jitter expression). In the simulation, the stellar rotation period is a known quantity. To generally address the planetary orbital period, we talk about the ratio relative to one stellar rotation. For example, the planetary orbital frequency to stellar rotation frequency ratio is set to be 0.7 (i.e. $\nu_{\text{orb}}/\nu_{\text{rot}} = P_{\text{rot}}/P_{\text{orb}} = 0.7$).

We then obtained three sets of radial velocities for each simulated profile: RV_{Gaussian}, $RV_{\text{FT,H}}$ and $RV_{\text{FT,L}}$ (Fig. 2.13 upper panel). We tested three different combinations of w_1 and w_2 in Eq. 2.18: (1) $w_1 = 1, w_2 = 0$; (2) $w_1 = 0.5, w_2 = 0.5$; (3) $w_1 = 0, w_2 = 1$, each is multiplied by their respective scaling factor (fitted by linear regression to the known input jitter) to see how well it matches the input jitter. The middle panel demonstrates a consistent recovery of jitter among the three expressions of jitter model, albeit with small differences. A weighted moving average was applied to show the trend. The lower panel is the residual of the fitting, with the weighted moving average on top.

To quantitatively examine the performance of the jitter models, we compare the scatter of data before and after the jitter model is applied (i.e. middle and bottom panels of Fig. 2.13). The scatter due to jitter is $\sigma_{\text{jitter}} = 1.22$ m/s (orange dashed line in the middle panel), and the scatter of residuals can be found in Table 2.2, mainly depending on the S/N and whether and how smoothing is adopted. In addition to the high S/N (= 10,000) simulations [1], we also simulate a moderate noise condition: S/N = 2,000 [2].

	σ_{residual} (raw) [m/s]		σ_{residual} (smoothed) [m/s]	
	S/N=10,000	S/N=2,000	S/N=10,000	S/N=2,000
$w_1 = 1, w_2 = 0$	0.72	2.51	0.46	0.74
$w_1 = 0.5, w_2 = 0.5$	0.69	2.07	0.51	0.64
$w_1 = 0, w_2 = 1$	0.69	2.20	0.48	0.68

Table 2.2: Residuals after applying our jitter model (in comparison with $\sigma_{\text{jitter}} = 1.22$ m/s)

We note from the table, that the scatter due to the simulated jitter is reduced from $\sigma_{\text{jitter}} = 1.22$ m/s to $\sigma_{\text{residual}} \sim 0.70$ m/s for S/N=10,000, but increased to 2.0 - 2.5 m/s for S/N=2,000. Implementing the weighted moving average with a meaningful correlation time-scale τ can further reduce σ_{residual}. In this exercise, we choose the time-scale for S/N=10,000 to be twice the spacing between two subsequent simulated observations, and for S/N=2,000 5 times the spacing. We also tested other smoothing approaches, such as the Python `PyMC3` implementation of Gaussian process smoothing, with similar results.

We note that after jitter correction, the residuals σ_{residual} are still larger than that from simulations without planets (§ 2.2.2). This is not because the presence of a planet alters the residuals, but rather die to the different ways in which jitter was dealt with. In § 2.2.2, we know our simulations have no planets, so that the measured $RV_{\text{FT,H}}$ and $RV_{\text{FT,L}}$ are solely proportional to the input jitter (scaling factor ~ 0.7 and ~ 1.3 respectively). In reality, we have no idea if there are planets in the system, so to construct the jitter model is first to remove the contributions from planets (E.q. 2.15

[1] This is the typical S/N found in the cross-correlation line profiles of HARPS observations of α Cen B.

[2] S/N ranging from 2,000 to 4,000 are found in a dwarf star HD 189733 with apparent magnitude $V = 7.6$; lower S/N$\sim$1,000 are found for red dwarfs Gl 176 and Wolf 1061 with $V \sim 10$.

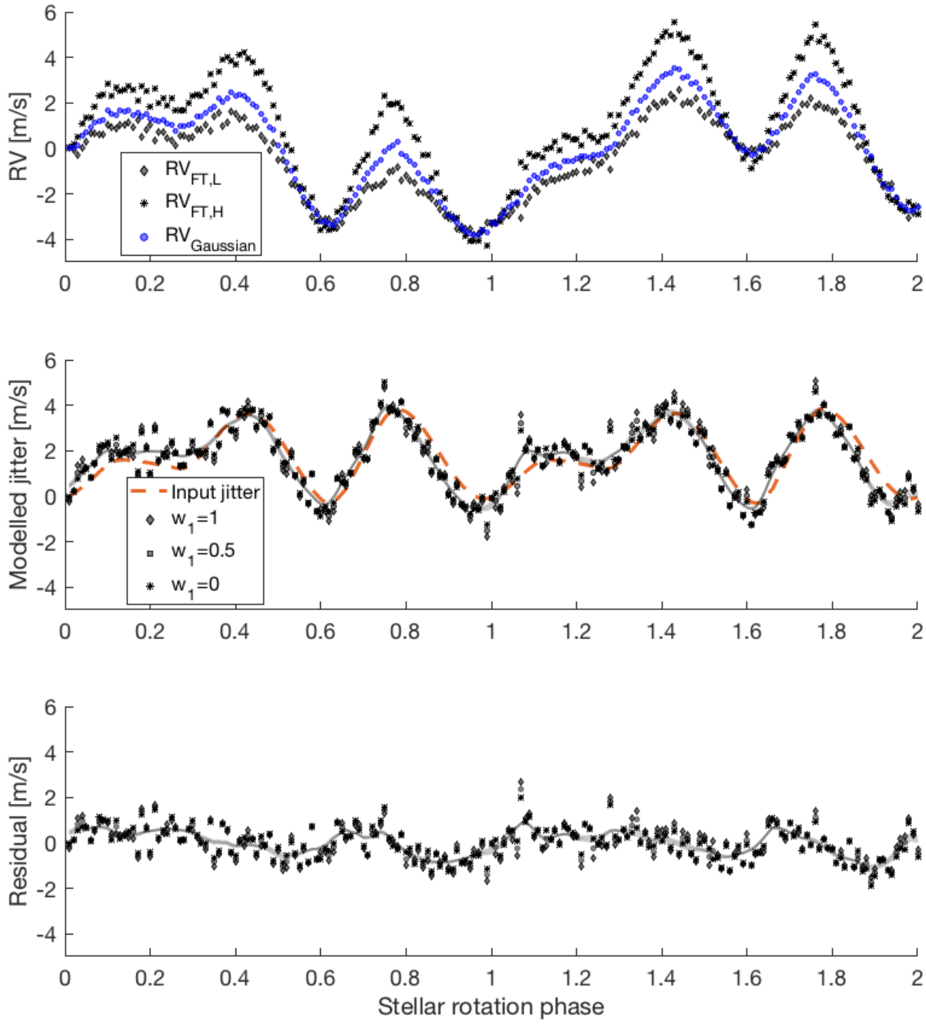

Fig. 2.13: Jitter recovery based on Eq. 2.18 for simulated data with S/N = 10,000. Top: time series of directly measured $RV_{\rm Gaussian}$, $RV_{\rm FT,L}$ and $RV_{\rm FT,H}$. Middle: three forms of jitter ($w_1 = 1, 0.5$ and 0) scaled to match the input jitter, and smoothed by the weighted moving average (grey solid lines) with τ equal to the spacing of two samplings to show the trend of the recovered jitter. For comparison, the input jitter is labelled as the orange dashed line. Bottom: difference between the jitter model and the input jitter, smoothed by the weighted moving average (grey solid lines). Differences between the three expressions for jitter are small (...). Note the scaling across the three subplots are the same.

24

and 2.16). Doing so requires scaling ΔRV_{H} and ΔRV_{L} by a factor of 2 - 4, and thus increasing the scatter of residuals.

In conclusion, we have demonstrated sub-m/s results for the residuals after implementing a jitter correction derived from ΦESTA. This indicates the potential to enhance the detection of planets at sub-m/s precisions and reveal candidates with radial velocities of sub-m/s amplitudes in the presence of stellar variability. However, this does require good data sampling and moderate-to-high S/N data.

2.2.6 Planetary radial velocity recovery

Having obtained the jitter model (Eq. 2.18) and assuming RV_{planet} follows a Keplerian orbital motion, we can turn our planetary radial velocity recovery into a model fitting problem, in which the parameters of the jitter model (such as the scaling factor) and that of the Keplerian orbit (such as amplitude, orbital period and phase) need to be determined.

Alternatively, we can bypass the jitter model. Revisiting the Equations 2.10-2.12, we rewrite them by observation number $i (i = 1, 2, \ldots, N)$ and switch the notation to obtain the following $3N$ independent linear equations:

$$X_i = P_i + J_i \tag{2.21}$$

$$Y_i = P_i + k_y \cdot J_i \tag{2.22}$$

$$Z_i = P_i + k_z \cdot J_i \tag{2.23}$$

where X_i, Y_i and Z_i replace the three measurable radial velocities RV_{Gaussian}, $RV_{\mathrm{FT,L}}$ and $RV_{\mathrm{FT,H}}$; P_i and J_i are the planetary and the jitter radial velocities; and k_y and k_z are the scaling factors k_L and k_H. Substituting $J_i = X_i - P_i$ from Eq. 2.21, we can simplify the system to $2N$ independent linear equations:

$$Y_i = k_y \cdot X_i + (1 - k_y) P_i \tag{2.24}$$

$$Z_i = k_z \cdot X_i + (1 - k_z) P_i. \tag{2.25}$$

The number of unknowns is $(N + 4)$, including N from P_i, 2 from k_y and k_z, and another 2 from the previously absorbed constant offsets. Normally we have $N \gg 1$, so that the number of independent equations ($2N$) is larger than the number of degrees of freedom ($N + 4$) in the system, meaning the system can be uniquely solved by optimization, such as least square minimization of the objective function:

$$\sum_{i=1}^{N}\left[w_{y,i}\Big(k_y \cdot X_i + (1-k_y)P_i - Y_i\Big)^2 + w_{z,i}\Big(k_z \cdot X_i + (1-k_z)P_i - Z_i\Big)^2\right] \tag{2.26}$$

where $w_{y,i}$ and $w_{z,i}$ are pre-determined weights (e.g. determined by the sizes of errorbars of the observed radial velocities). This approach becomes identical to constructing a jitter model (Eq. 2.18) in cases where (1) $w_{y,i} = 1, w_{z,i} = 0 (i = 1, 2, \ldots, N)$ and $w_1 = 1, w_2 = 0$; (2) $w_{y,i} = 0, w_{z,i} = 1 (i = 1, 2, \ldots, N)$ and $w_1 = 0, w_2 = 1$.

2.2.7 Conclusion

Fourier phase spectrum analysis ($\varPhi$ESTA or FIESTA) can be used to combine information from the power and phase spectra to return radial velocities consistent with those acquired by fitting a Gaussian function to a line profile. This conclusion applies both for measuring a direct line shift and an apparent shift of a deformed line profile.

The frequency dependent $x_0(\xi)$ is the key asset in identifying line profile deformation and distinguishing it from a bulk line shift. We have investigated the apparent radial velocity shift (i.e. jitter) produced by deformed line profiles and shown it can be considered as the combination of two radial velocities – $RV_{\mathrm{FT,H}}$ in higher frequency modes and $RV_{\mathrm{FT,L}}$ in lower frequency modes. They both correlate linearly with jitter (as obtained from the simulated spectral line profiles).

The different strengths of these correlations for $RV_{\mathrm{FT,H}}$ and $RV_{\mathrm{FT,L}}$ enable us to calculate the jitter matrices and construct a jitter model, which can recover simulated radial velocities data when combined with stellar variability, in both high-and-moderate S/N simulations.

2.3 End-to-end simulations

We ran end-to-end simulations to test the performance of ΦESTA for recovering a planetary signal in the presence of jitter. Specifically, we sought to answer the following three questions:

1. When the amplitude of jitter is comparable to that of planetary radial velocities, can we better recover the planet orbital parameters with ΦESTA?
2. When planetary radial velocities dominate and jitter is negligible, does ΦESTA give at least equally good results as traditional methods (i.e. without jitter correction)?
3. When jitter is the only source of radial velocity variation, can it be identified with the help of ΦESTA?

For all the following simulations, the spectral line profile simulator (SOAP 2.0) setup is the same as previously. The jitter amplitude is fixed at roughly 2 m/s, so we will adjust the planetary orbital amplitude to satisfy the three categories of end-to-end simulations. For S/N, we choose two numbers to represent the simulations: (1) S/N = 10,000 where we show its ability of significantly improving the detection of planets orbiting bright and active stars; (2) S/N = 2,000 where it starts to push the limit of ΦESTA. We will run 500 trails, each trail with 60 randomly selected samples clustered in 12 groups, out of a total of 400 equally spaced samples from four stellar rotation periods.

The tests are divided into two main groups for comparison:

1. Fit RV_{Gaussian} by Keplerian orbit alone;
2. Fit RV_{Gaussian} by Keplerian orbit with jitter model correction. The following three variations of model fitting have been tested:
   (a) Jitter model constructed with RV_{Gaussian} and $RV_{\text{FT,L}}$ only, i.e. $w_1 = 1$ and $w_2 = 0$;
   (b) Jitter model constructed with RV_{Gaussian} and $RV_{\text{FT,H}}$ only, i.e. $w_1 = 0$ and $w_2 = 1$;
   (c) Jitter model constructed with RV_{Gaussian}, $RV_{\text{FT,L}}$ and $RV_{\text{FT,H}}$, represented by $w_1 = 0.5$ and $w_2 = 0.5$ in our test.

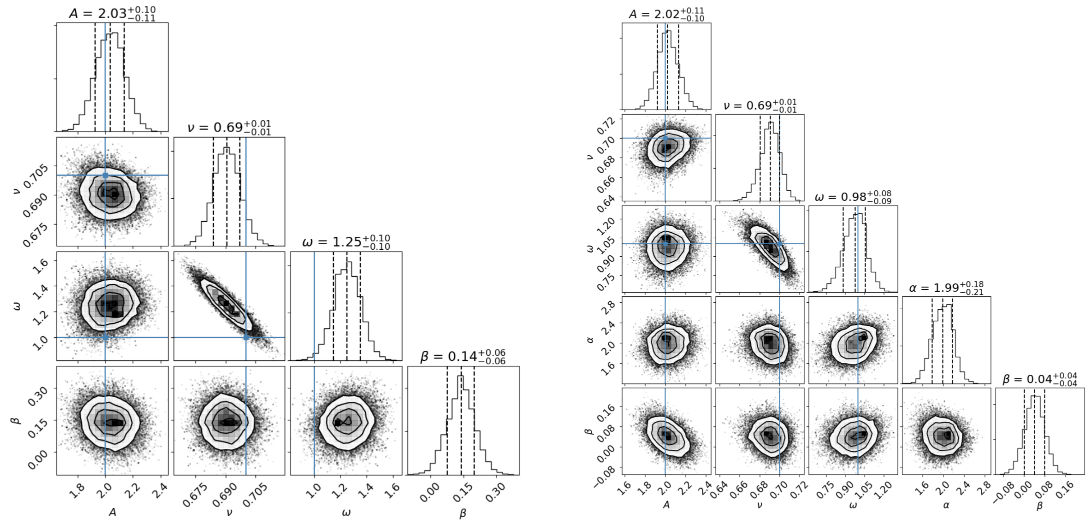

(a) No jitter correction

(b) Jitter correction applied

Fig. 2.14: Examples of two corner plots showing the successfully recovered planetary orbital parameters (within 5% of the true values for A and ν) with MCMC sampling. The blue solid lines indicate the true values of the input orbital parameters. The three dashed lines of each histogram are the corresponding median and 1σ boundaries. A, ν, ω, α and β are the orbital amplitude, orbital frequency ratio, initial phase, the scaling factor for the jitter term and a radial velocity offset respectively.

The parameters for the fitting is obtained by Markov chain Monte Carlo (MCMC) sampling (such as shown in Fig. 2.14). Each radial velocity data is equally weighted as they have the same S/N in our simulation. We find that among the three variations of jitter correction treatments, the one left with the least residual (i.e. smallest rms) empirically returns the best fitting parameters, which we would use to represent the fitting from Group 2.

We have done some test end-to-end simulations to investigate if the choice of the dividing frequency ξ_{HL}, or if having an overlapping frequency range such that $RV_{\mathrm{FT,L}}$ is contributed by [0, ξ_{HL1}] and $RV_{\mathrm{FT,H}}$ by [ξ_{HL2}, ξ_H] in which $\xi_{HL1} > \xi_{HL2}$, would make a difference in the overall performance of planet recoveries. Instead of equally dividing the power spectrum into the higher and lower frequencies as in the previous demonstrations, ξ_{HL} chosen roughly one third of the cut-off frequency (resulting in about 85% of power goes to $RV_{\mathrm{FT,L}}$ and the other 15% goes to $RV_{\mathrm{FT,H}}$) tends to improve the successful recovery rate better than the other cases that we have tested and thus is used in the end-to-end simulations presented in this subsection. However, we have not drawn solid conclusions on a sweet spot for ξ_{HL}.

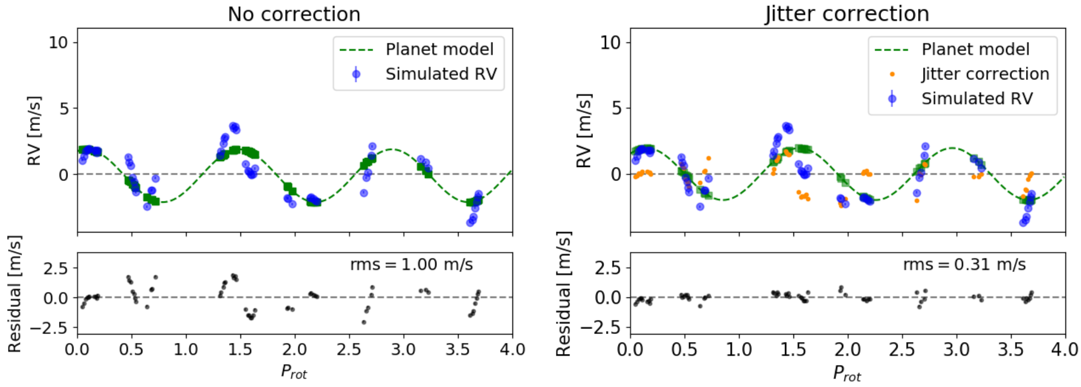

(a) S/N = 10,000

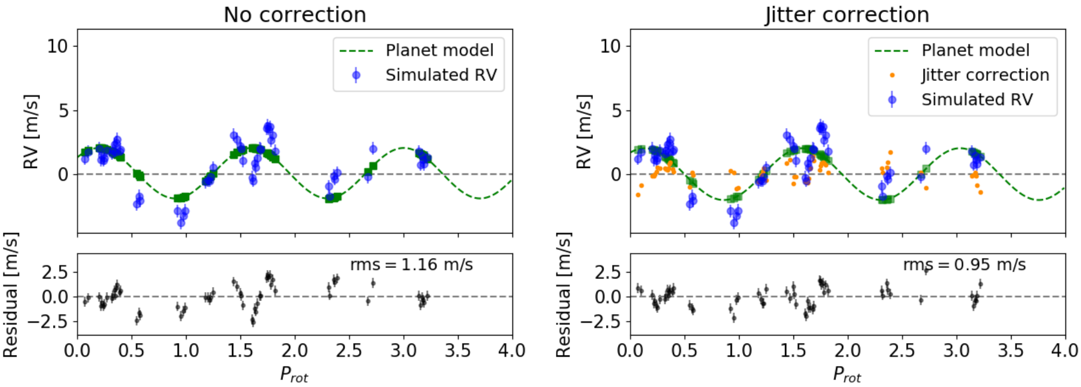

(b) S/N = 2,000

Fig. 2.15: One of the 500 trails of radial velocity fitting for $A = 2$ m/s for S/N = 10,000 and 2,000 respectively.

2.3.1 Stellar jitter amplitude ≈ planetary amplitude

The injected planet has the same parameter settings as in §2.2.5, i.e. circular orbit with amplitude $A = 2$ m/s, orbital frequency ratio $\nu = \nu_{\text{orb}}/\nu_{\text{rot}} = 0.7$ and initial phase $\omega = 1$ rad. For demonstration, we present two snapshots of each of the 500 trails of end-to-end simulations, with one S/N = 10,000 and the other S/N = 2,000 (Fig. 2.15). These are two examples where the planetary orbital parameters are correctly recovered (within 10% of the true values in this case). For S/N = 10,000, the discrepancy between the simulated radial velocities and the planet model is accounted for by the jitter model, and thus applying the jitter correction significantly reduces the rms of the residual. For S/N = 2,000, the fitting is only slightly improved introducing jitter correction. The jitter model is not as accurate in the presence of moderate noise.

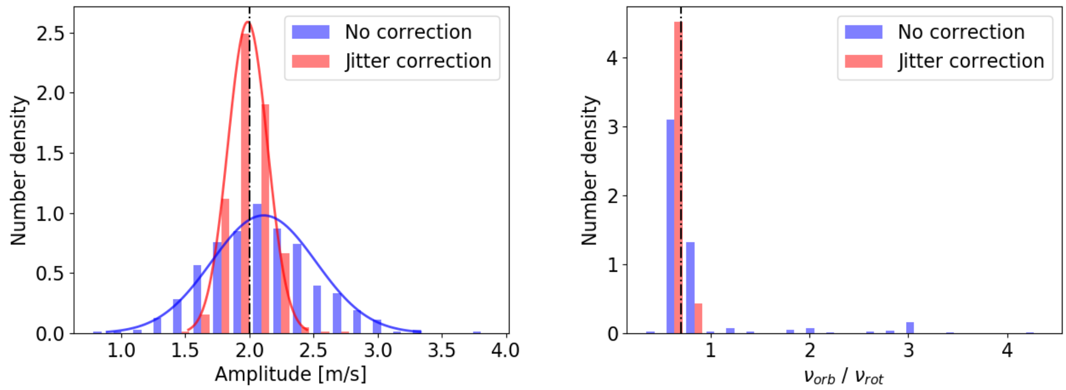

(a) S/N = 10,000

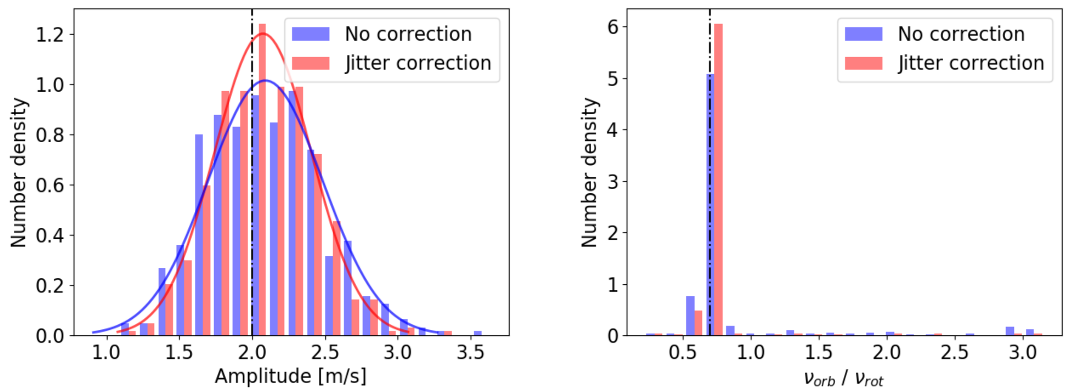

(b) S/N = 2,000

Fig. 2.16: Histograms of recovered orbital parameters with a Gaussian profile fitted on top (where applicable).

In the end, we obtain the histograms of the recovered orbital parameters for a total of 500 runs (Fig. 2.16). To quantitatively describe their performances, we calculate the percentage of parameters successfully recovered within 5% and 10% of the true values as summarized in Table 2.3. For example, for S/N = 10,000, 46% of the 500 trails have both the amplitude (A) and orbital frequency ($\nu_{\mathrm{orb}}/\nu_{\mathrm{rot}}$) successfully recovered within 5% of the true parameters with jitter correction applied, while only 8% of them achieve such a precision without jitter correction.

Percentage	S/N = 10,000				S/N = 2,000			
	5% limit		10% limit		5% limit		10% limit	
	†	‡	†	‡	†	‡	†	‡
A	18%	50%	37%	79%	20%	23%	37%	42%
$\nu_{\mathrm{orb}}/\nu_{\mathrm{rot}}$	53%	93%	78%	100%	49%	66%	77%	91%
both A and $\nu_{\mathrm{orb}}/\nu_{\mathrm{rot}}$	8%	46%	27%	79%	10%	16%	28%	38%

Table 2.3: Proportion of recovered parameters within 5% and 10% limit of $A =$ 2 m/s and $\nu_{\mathrm{orb}}/\nu_{\mathrm{rot}} = 0.7$. †: no correction; ‡: jitter correction applied.

2.3.2 Planetary signal dominates

In this case, we set the orbital amplitude roughly 10 times as strong as the jitter, i.e. $A =$ 20 m/s (Fig. 2.17). Although both with and without the aid of jitter correction manage to recover the planetary orbital parameters accurately enough, implementing *Φ*ESTA further improves the performance, especially in high S/N (Fig. 2.18 and Table. 2.4).

Percentage	S/N = 10,000				S/N = 2,000			
	1% limit		5% limit		1% limit		5% limit	
	†	‡	†	‡	†	‡	†	‡
A	33%	61%	99%	100%	34%	40%	98%	100%
$\nu_{\mathrm{orb}}/\nu_{\mathrm{rot}}$	92%	100%	100%	100%	93%	96%	100%	100%
both A and $\nu_{\mathrm{orb}}/\nu_{\mathrm{rot}}$	30%	61%	99%	100%	31%	38%	98%	100%

Table 2.4: Proportion of recovered parameters within 1% and 5% limit of $A =$ 20 m/s and $\nu_{\mathrm{orb}}/\nu_{\mathrm{rot}} = 0.7$. †: no correction; ‡: jitter correction applied.

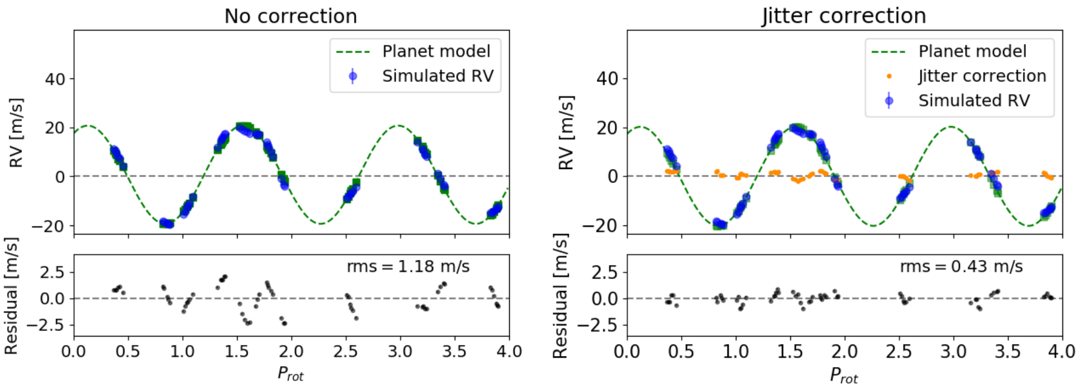

(a) S/N = 10,000

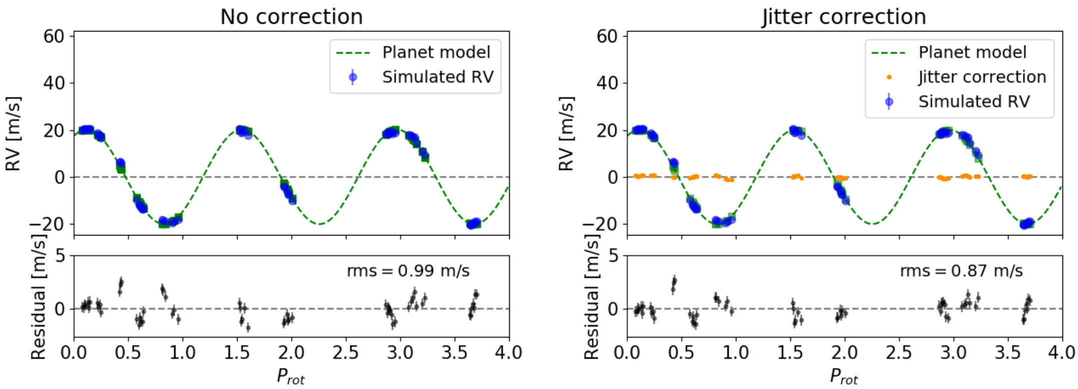

(b) S/N = 2,000

Fig. 2.17: Same with Fig. 2.15 but for $A = 20$ m/s.

32

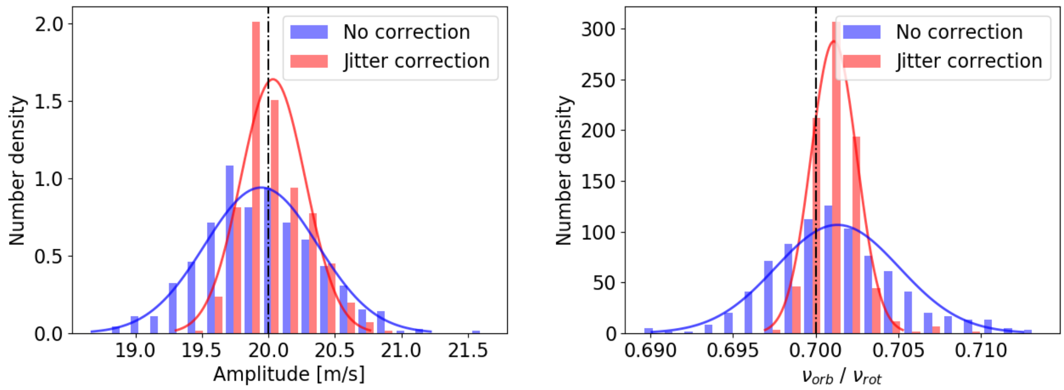

(a) S/N = 10,000

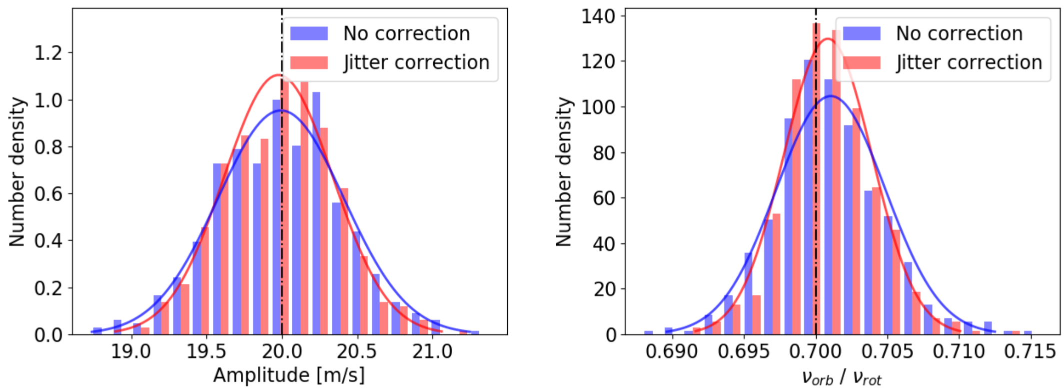

(b) S/N = 2,000

Fig. 2.18: Same with Fig. 2.16 but for $A = 20$ m/s.

2.3.3 Stellar jitter only

We set $A = 0$ m/s so that the measured the radial velocity only comes from stellar variability. We implement the same approaches as above to see if the applying the jitter correction can return a null planet solution i.e. recovered amplitude smaller than the noise level.

We remind ourselves that the spot configuration in Table 2.1 is used. Three starspots appear and diasppear in turns (Fig. 2.10), mimicking the radial velocities of orbiting exoplanets. This is indeed the case in the histogram of "recovered" orbital parameters (Fig. 2.19) – three peaks occur at $\nu_{\rm orb}/\nu_{\rm rot} = 1$, 2 and 3, with $\nu_{\rm orb}/\nu_{\rm rot} = 3$ being the most prominent. Applying the jitter correction, the amplitudes of the "recovered" planet for S/N = 10,000 is effectively reduced, but its performance is only marginally better for S/N = 2,000, and neither of them reaches below the rms of photon noise level: ~ 0.1 m/s for S/N = 10,000 and ~ 0.5 m/s for S/N = 2,000. We still cannot completely rule out the possibility of a reduced amplitude being true. Therefore, we come up with the following two subsections to discuss how we can classify whether the planetary signal or the stellar jitter dominates the observed radial velocities.

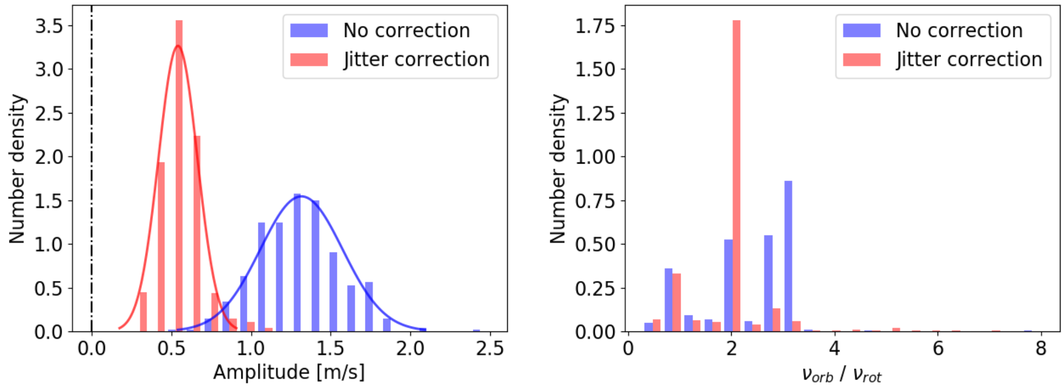

(a) S/N = 10,000

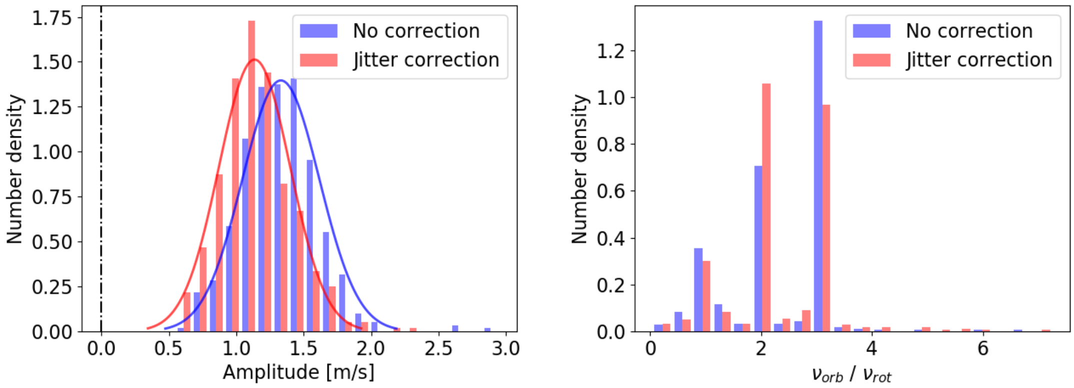

(b) S/N = 2,000

Fig. 2.19: Histogram of "recovered" orbital parameters in null planet end-to-end simulations.

2.3.4 Classification

We demonstrate the use of the relations among RV_{Gaussian}, $RV_{\mathrm{FT,H/L}}$ and $\Delta RV_{\mathrm{H/L}}$ to classify if a system is dominated by jitter and planetary signals (Fig. 2.20). The common feature in (a), (b) and (c), where stellar jitter is present, is a well defined linear correlation between ΔRV_{H} and ΔRV_{L}. Both ΔRV_{H} and ΔRV_{L} are used as jitter indicators. They are linearly correlated with jitter and thus proportional to each other as well. The different features in each of the four panels are:

(a) Stellar jitter as strong as planetary signals –

(b) another item

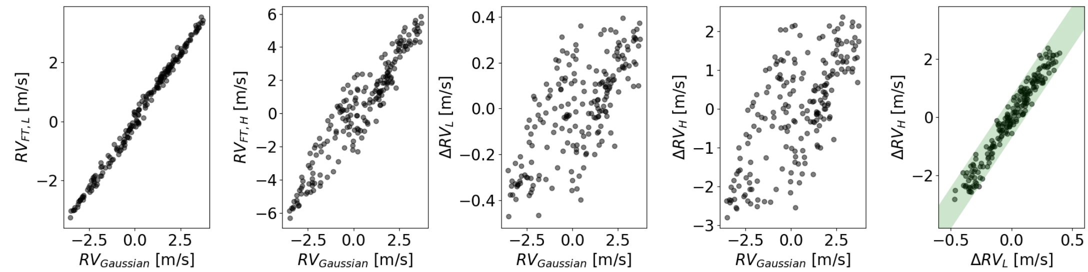

(a) Stellar jitter as strong as planetary signal: featured by (1) a decent correlation between $RV_{\rm Gaussian}$ and $RV_{\rm FT,L}$ and (2) no correlation between $RV_{\rm Gaussian} - RV_{\rm FT,H/L}$.

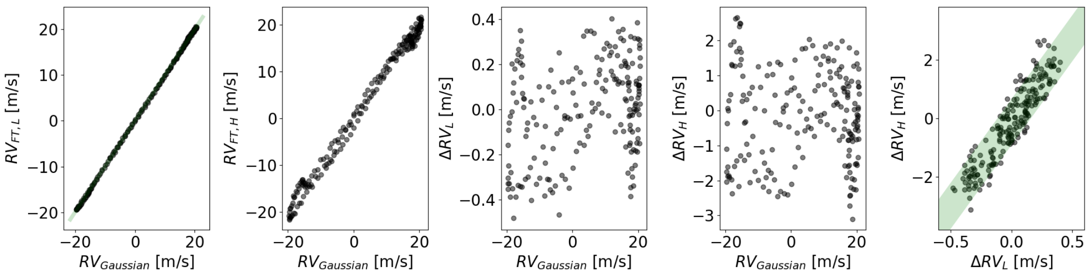

(b) Planetary signal dominating: featured by (1) a tight correlation between $RV_{\rm FT,L}$ and $RV_{\rm Gaussian}$ and (2) no correlation between $RV_{\rm Gaussian} - RV_{\rm FT,H/L}$.

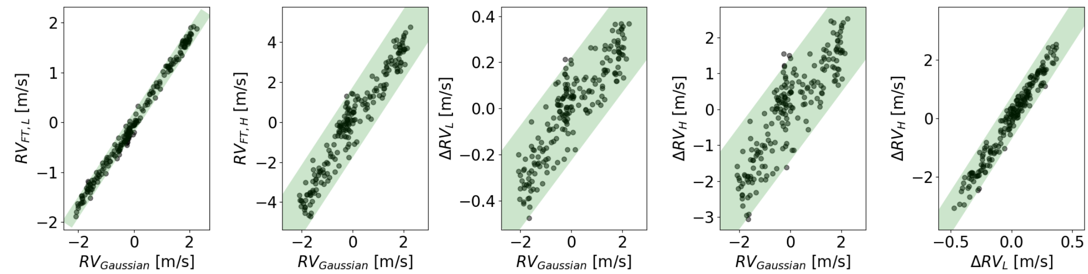

(c) Jitter only; no planet: featured by linear correlations in all the subplots, on which ΦESTA are based.

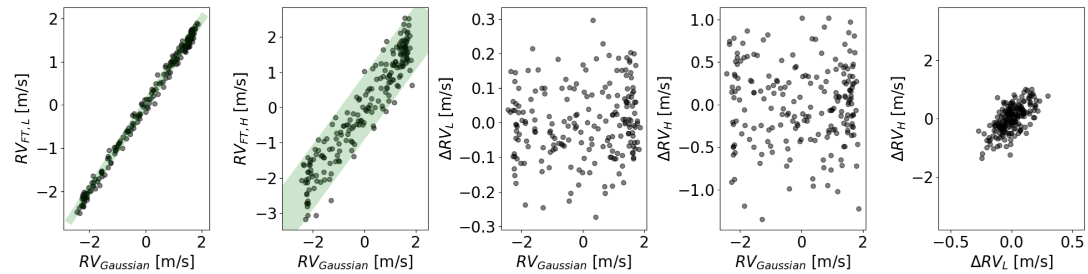

(d) Planet only; "no" jitter. No apparent difference from (a) at first sight. This is because ΦESTA cannot tell whether the difference between line profiles are due to what we define as stellar jitter or the fluctuation from photon noise, but notice the scales of $RV_{\rm FT,H,L}$ in (d) are different from (a), because $RV_{\rm FT,H} \approx RV_{\rm FT,L} \approx RV_{\rm Gaussian}$ without the presence of jitter.

Fig. 2.20: Classification of a system whether it's jitter dominated or planetary signal dominated.

2.3.5 Periogodgram combined with the ΦESTA

We would use the generalized Lomb-Scargle periodogram [2] in combination with ΦESTA to address the problem of stellar jitter mimicking planetary signals. The idea is to compare the periodogram of the measured radial velocity (i.e. RV_{Gaussian}) and that of the proto-jitter (i.e. $\mid RV_{\mathrm{FT,H/L}} - RV_{\mathrm{Gaussian}} \mid$). Peaks of the periodogram in the former are possible candidates whereas the latter would indicate jitter.

Fig. 2.21 demonstrates the application of periogodgram together with ΦESTA, on the well sampled radial velocities (without sub-sampling) from the two end-to-end simulations in §2.3: (1) stellar jitter as strong as planetary signal and (2) stellar jitter only. The S/N of the cross-correlation profile is 2000 and because we used a full range of sampling, no moving average was applied. In Fig. 2.21a the planetary orbital frequency $\nu_{\mathrm{orb}}/\nu_{\mathrm{rot}} = 0.7$ clearly stands out while the other peaks coincide with that of the proto-jitter. It effectively shows, the proto-jitter model generated by ΦESTA manages to disentangle jitter from the planetary component of the radial velocities (we recall that the planetary radial velocity was cancelled out to construct the jitter model). In the case of a null planet (Fig. 2.21b), all the possible candidates where the RV_{Gaussian} peaks occur are negated by the same detected periodicity of the jitter.

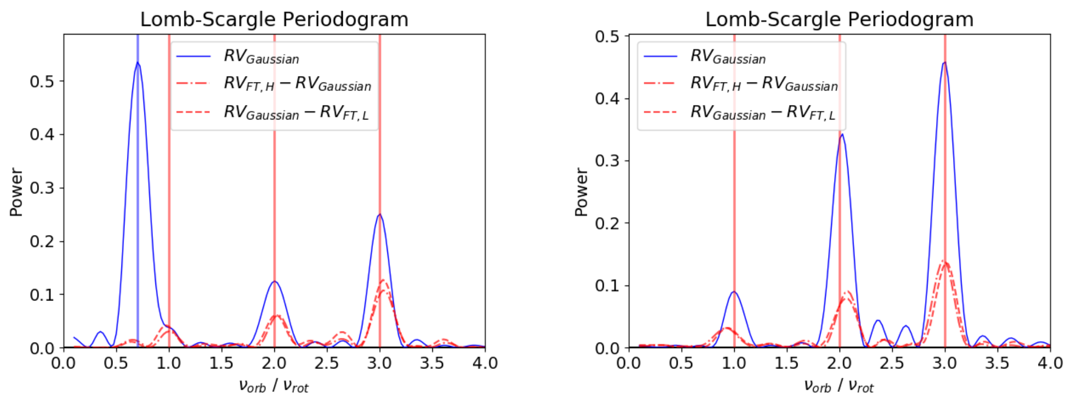

(a) Stellar jitter as strong as planetary signal   **(b)** Stellar jitter only

Fig. 2.21: Periodogram of RV_{Gaussian} and $\mid RV_{\mathrm{FT,H/L}} - RV_{\mathrm{Gaussian}} \mid$. The single prominent peak in (a) indicates the orbital frequency (or period) of the injected planet. The true orbital frequency is labelled as the blue vertical line; the suspicious frequencies are labelled in red vertical lines at $\nu_{\mathrm{orb}}/\nu_{\mathrm{rot}} = 1$, 2 and 3.

2.4 Applying ΦESTA on real observations

2.4.1 HD189733: Rossiter–McLaughlin effect as jitter

HD189733 is a well studied binary star system. The main star HD189733 A is known to host a gas giant exoplanet HD189733 b, first detected by transits and followed by Doppler spectroscopy conformation [3]. Its Rossiter–McLaughlin effect (Fig. 2.22), as a change in radial velocities when the planet passes in front of its parent star, was studied by [4] and [5]. During the eclipse, the planet breaks the observed flux symmetry of the stellar photosphere, resulting in imbalanced redshift and blueshift, producing an asymmetric spectral line profile and apparent radial velocity shifts.

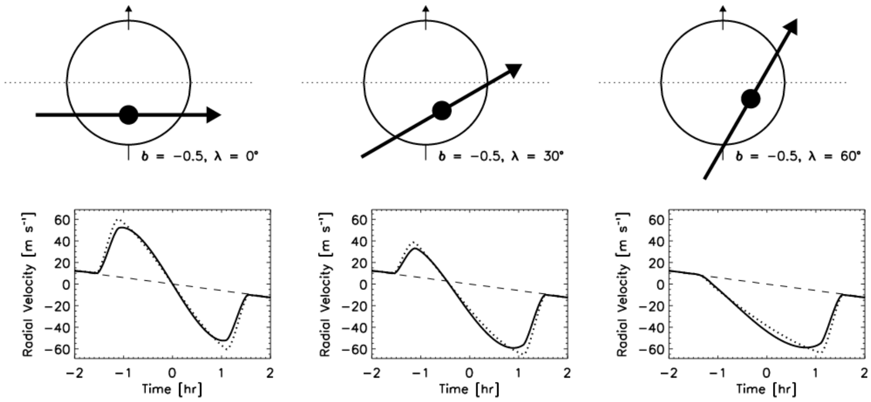

Fig. 2.22: Demo: Rossiter–McLaughlin effect (figure taken from [6]). It is an apparent radial velocity change of the parent star due to an eclipsing binary (whether star or planet) in front of the stellar photosphere. It shows in this plot three different star-planet alignments that cause three corresponding different forms of Rossiter–McLaughlin curves. Solid line is the model with limb darkening as opposed to dotted line without limb darkening.

We aim to test if our jitter model generateed by ΦESTA can account for the apparent radial velocity shift as a result of Rossiter–McLaughlin effect. We choose this target as a case study for the following reasons: (1) HD189733 b is a confirmed transiting exoplanet, so that we know what to expect from the radial velocity shift during the eclipse. (2) The gas giant exoplanet causes a prominent apparent radial velocity shift while it transits (amplitude up to $\sim$ 40 m/s) arising from Rossiter–McLaughlin effect, making it the dominant factor of the radial velocity shift, although the star itself exhibits signs of activity ([7], [8]). (3) The system HD189733 has a visual magnitude of $V \sim 7.65$ [9] (or $G = 7.41$ from the Gaia archive), dominated by the primary host

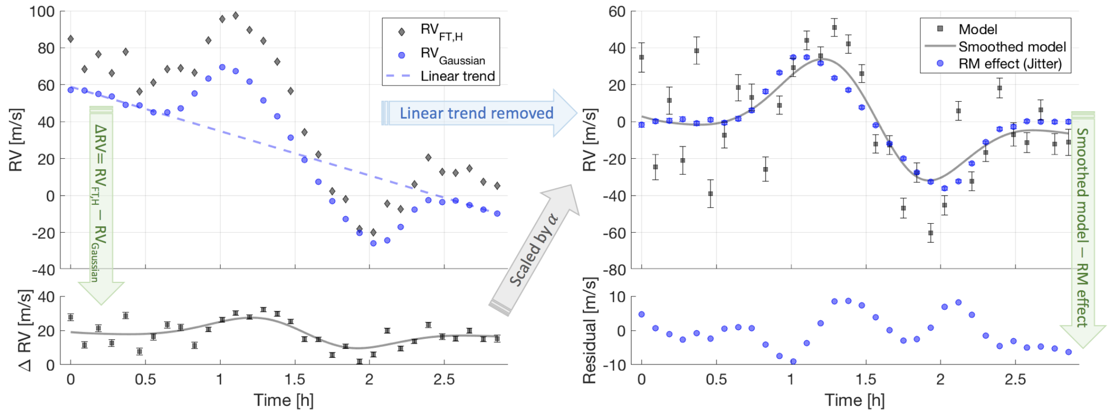

Fig. 2.23: Flowchart of modelling Rossiter–McLaughlin effect as jitter using ΦESTA on HD189733. Note that the errorbars related to the radial velocities from ΦESTA (e.g. the scaled raw jitter in the top right panel) are correct in scale relative to each other (as derived from the photon noise) but not evaluated in the absolute value.

star HD189733 A, with a relatively high S/N in the HARPS cross-correlation profile, enabling decently good performance of ΦESTA in recovering radial velocities.

Here we briefly recap the procedure of obtaining the "jitter" model by ΦESTA. Both RV_{Gaussian}, $RV_{\mathrm{FT,H}}$ and $RV_{\mathrm{FT,L}}$) are calculated from the HARPS cross-correlation of the spectral lines. Note that RV_{Gaussian}, RV_{HARPS} and RV_{FT} deliver consistent radial velocities, and thus in practice, it barely makes difference to adopt any of them as the radial velocity shift of the line profile. We calculate $\Delta RV = \mid RV_{\mathrm{Gaussian}} - RV_{\mathrm{FT,H/L}} \mid$ as the raw proto-jitter (Fig. 2.23 bottom left). We know that during transit, the orbital phase of the planet HD189733 b is zero and thus contributes no radial velocity, however, the inclined trend of the radial velocity curve is attributed to the exoplanet whose orbital period is estimated 11 days [3], as well as the other star HD189733 B in the binary star system of which the orbital period is estimated around 3,200 years [10], both being reasonably long enough as opposed to the time-scale of the planetary transit of hours, therefore a local linear approximation can be applied by fitting a linear trend onto the non-transiting part of the radial velocities as the orbital radial velocities, which is then removed and left with the Rossiter–McLaughlin curve (Fig. 2.23 top right). It can be now treated as "jitter" and modelled by the raw proto-jitter multiplied by a scaling factor (Fig. 2.23 right).

For this exercise, the scaled model is smoothed by the weighted moving average with $\tau \sim 0.2$ hour, twice of the spacing of two consecutive observations. Despite mitigating against additional noise brought by *Φ*ESTA, it smears the drastic velocity change when the planet ingresses and egresses the stellar disk. Applying a correct Rossiter–McLaughlin curve model is expected to improve the fitting, we still adopt the smoothing approach the way we would normally (intend to) deal with stellar variability induced radial velocities instead, to demonstrate the sufficiently recovered radial velocities as a result of line profile deformation – a 75% removal of the "jitter" from ~ 40 m/s to ~ 10 m/s.

2.4.2 α Centauri B (HD128621)

We chose α Centauri B as our case study for its brightness (V$\sim$1.33), abundant HARPS observations, and the controversy over whether it hosts an exoplanet due to its intrinsic stellar activity. Being potentially the (second) closest exoplanet to Earth, the candidate α Centauri B was first discovered by [11] in 2012, then further investigated by [12] in 2013, and later questioned by [13], suggesting it was a detection of a ghost signal arised from the window function. We haven't gone as far as probing the spurious planetary candidate, but we could study is the stellar activity level of α Centauri B, presented by a scaled jitter correction $\Delta RV_{\mathrm{H/L}} = \mid RV_{\mathrm{HARPS}} - RV_{\mathrm{FT,H/L}} \mid$. In the following, we focus on three segments of the α Centauri B data sets for activity analysis, each roughly one year apart, spanning within three months and including over 2000 observations. Epoch 1: 15/02/2009 - 06/05/2009; Epoch 2: 03/23/2010 - 12/06/2010; Epoch 3: 18/02/2011 - 15/05/2011. Among them, Epoch 2 is of particular interest as it has been used to study rotationally modulated stellar activities in K-dwarfs ([14], [15]).

We downloaded 2617 α Centauri B spectra for Epoch 2 (2010) from the ESO archive, from which we selected the 2529 cross-correlation line profiles that were constructed with a K5 stellar template; the number of observations actually used was then further reduced to 2488 as we took out another 41 observations that presented large radial velocity offsets and visually different cross-correlation line profiles from the rest of the profiles. These removed observations had features at ephemeral time-scales, i.e. their radial velocities stood out from the other observations of the same day in the RV_{HARPS} or $\Delta RV_{\mathrm{H/L}}$ time-series and they were also classified as outliers in the full width at half maximum (FWHM) indicator, suggesting the presence of stellar flares. Epoch 1 (2009) and 3 (2011) were pre-filtered in a similar manner, resulting in 2220 and 3534 observations used respectively.

Fig. 2.24 presents the results of ΦESTA analysis of $\Delta RV_{\mathrm{L}} = RV_{\mathrm{HARPS}} - RV_{\mathrm{FT,L}}$ for these 3 years. $\Delta RV_{\mathrm{H}} = RV_{\mathrm{FT,H}} - RV_{\mathrm{HARPS}}$ is not shown here as it is simply proportional to ΔRV_{L} and works the same way. We fit ΔRV_{L} with a Gaussian process model described by a quasi-periodic kernel. A Gaussian process model has the advantage of interpreting stochastic processes with a set of flexible forms of functions, constrained by physically motivated covariance kernels. In this case, a quasi-periodic kernel was chosen such that the periodicity can be explained by the rotationally modulated activity and the deviation from periodicity explained by possibly self-evolving disc features (e.g. starspots and plage, differential rotation). Interested readers can refer the theoretical background of Gaussian processes to a textbook-like literature [16] or a hitchhiker's guide to Gaussian processes for time-series modelling [17]. For the implementation of the Gaussian process model, we employed the python library `george` delveloped by Foreman-Mackey [18].

The figure shows the star's activity level increased dramatically from 2009 (upper panel) to 2010 (middle panel), and then declined in 2011 (lower panel). It indicates in 2010, α Centauri B was dominated by a simple global feature on the stellar surface that appeared at a rotation period of around 40 days, while in 2009 and 2011 the star might be covered by various local features, making the disc inhomogeneous at smaller scales. A substantial literature have studied and even modelled the rotational activity in an attempt to pin down the exoplanet candidate α Centauri Bb, so that we can compare our results with them. The prominent periodicity in 2010 is found to be consistent with $\log(R'_{HK})$ in original discovery paper [11], as well as the equivalent widths and core flux of activity-sensitive Fe and Mg lines reported in [14] and [15]. While our scaled jitter correction ΔRV_{L} in Epoch 2 (2010) does not match with rotational activity fit from [11] and [12], we do find some similarities shared between our ΔRV_{L} in Epoch 3 (2011) and the corresponding trunk of rotational activity fit presented in [11] and [12], which were obtained using completely different methods from ours.

We obtained the stellar rotation period from the best fit solution with a quasi-periodic kernel. For the three phases that we studied from 2009 to 2011, the rotation period is estimated to be 37.05, 35.70 and 36.71 days, all within 1σ of the pre-claimed 36.2 ± 1.4 days [19]; the rotation period of Epoch 3 (2011) that we obtained is highly consistent with the one from [11]. Unsurprisingly, the other two periods are not, as our ΔRV_{L} model is different from the activity model fit in [11].

While , §2.3.4 has demonstrated ΦESTA does provide a quick assessment of whether a system hosts a planet / planets.

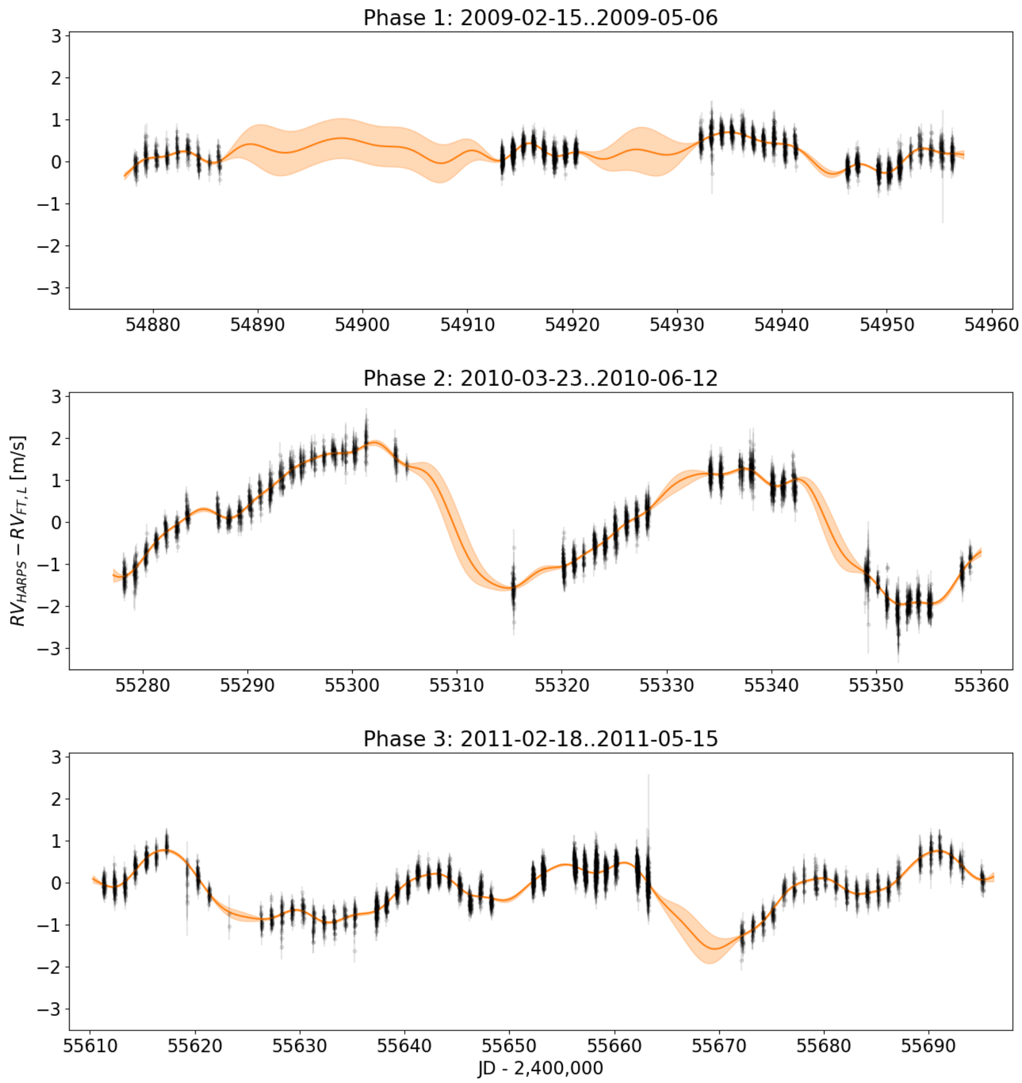

Fig. 2.24: Stellar activity analysis of α Centauri B using *Φ*ESTA. The scaling of the corresponding axes on all subplots are identical. Black dots with errorbars are radial velocities $RV_{\mathrm{HARPS}} - RV_{\mathrm{FT,L}}$; the orange solid line is the best fit solution with a quasi-periodic kernel using Gaussian processes and the shaded area is its 1σ boundary.

42

2.4.3 ϵ Eridani (HD22049)

2.4.4 τ Ceti (HD10700)

2.5 References

[1] X. Dumusque, I. Boisse, and N. C. Santos. Soap 2.0: A tool to estimate the photometric and radial velocity variations induced by stellar spots and plages. *The Astrophysical Journal*, 796(2):132, 2014. 8

[2] Zechmeister, M. and Kürster, M. The generalised lomb-scargle periodogram - a new formalism for the floating-mean and keplerian periodograms. *A&A*, 496(2):577–584, 2009. 37

[3] Bouchy, F., Udry, S., Mayor, M., Moutou, C., Pont, F., Iribarne, N., Da Silva, R., Ilovaisky, S., Queloz, D., Santos, N. C., Ségransan, D., and Zucker, S. Elodie metallicity-biased search for transiting hot jupiters - ii. a very hot jupiter transiting the bright k star hd189733. *A&A*, 444(1):L15–L19, 2005. 38, 39

[4] W. D. Cochran, M. Endl, R. A. Wittenmyer, and A. P. Hatzes. The Rossiter-McLaughlin Effect In Transits Of The Planet Hd189733b. In *AAS/Division for Planetary Sciences Meeting Abstracts #38*, volume 38 of *Bulletin of the American Astronomical Society*, page 481, September 2006. 38

[5] Triaud, A. H. M. J., Queloz, D., Bouchy, F., Moutou, C., Cameron, A. C., Claret, A., Barge, P., Benz, W., Deleuil, M., Guillot, T., Hébrard, G., Lecavelier des Étangs, A., Lovis, C., Mayor, M., Pepe, F., and Udry, S. The rossiter-mclaughlin effect of corot-3b and hd189733b. *A&A*, 506(1):377–384, 2009. 38

[6] B. Scott Gaudi and Joshua N. Winn. Prospects for the characterization and confirmation of transiting exoplanets via the rossiter-mclaughlin effect. *The Astrophysical Journal*, 655(1):550, 2007. 38

[7] Boisse, I., Moutou, C., Vidal-Madjar, A., Bouchy, F., Pont, F., Hébrard, G., Bonfils, X., Croll, B., Delfosse, X., Desort, M., Forveille, T., Lagrange, A.-M., Loeillet, B., Lovis, C., Matthews, J. M., Mayor, M., Pepe, F., Perrier, C., Queloz, D., Rowe, J. F., Santos, N. C., Ségransan, D., and Udry, S. Stellar activity of planetary host star hd 189733. *A&A*, 495(3):959–966, 2009. 38

[8] P. Wilson Cauley, Seth Redfield, and Adam G. Jensen. A decade of h alpha transits for hd 189733 b: Stellar activity versus absorption in the extended atmosphere. *The Astronomical Journal*, 153(5):217, 2017. 38

[9] C. Koen, D. Kilkenny, F. van Wyk, and F. Marang. Ubv(ri)cjhk observations of hipparcos-selected nearby stars. *Monthly Notices of the Royal Astronomical Society*, 403(4):1949–1968, 2010. 38

[10] Gáspár Á. Bakos, András Pál, David W. Latham, Robert W. Noyes, and Robert P. Stefanik. A stellar companion in the hd 189733 system with a known transiting extrasolar planet. *The Astrophysical Journal Letters*, 641(1):L57, 2006. 39

[11] Xavier Dumusque, Francesco Pepe, Christophe Lovis, Damien Ségransan, Johannes Sahlmann, Willy Benz, François Bouchy, Michel Mayor, Didier Queloz, Nuno Santos, and Stéphane Udry. An earth-mass planet orbiting α centauri b. *Nature*, 491:207 EP –, 10 2012. 40, 41

[12] Artie P. Hatzes. The radial velocity detection of earth-mass planets in the presence of activity noise: The case of alpha centauri bb. *The Astrophysical Journal*, 770(2):133, 2013. 40, 41

[13] V. Rajpaul, S. Aigrain, and S. Roberts. Ghost in the time series: no planet for alpha cen b. *Monthly Notices of the Royal Astronomical Society: Letters*, 456(1):L6–L10, 2016. 40

[14] A. P. G. Thompson, C. A. Watson, E. J. W. de Mooij, and D. B. Jess. The changing face of α centauri b: probing plage and stellar activity in k dwarfs. *Monthly Notices of the Royal Astronomical Society: Letters*, 468(1):L16–L20, 2017. 40, 41

[15] A. W. Wise, S. E. Dodson-Robinson, K. Bevenour, and A. Provini. New methods for finding activity-sensitive spectral lines: Combined visual identification and an automated pipeline find a set of 40 activity indicators. *The Astronomical Journal*, 156(4):180, 2018. 40, 41

[16] CE Rasmussen and CKI Williams. *Gaussian Processes for Machine Learning*. Adaptive Computation and Machine Learning. MIT Press, Cambridge, MA, USA, 1 2006. 41

[17] S. Roberts, M. Osborne, M. Ebden, S. Reece, N. Gibson, and S. Aigrain. Gaussian processes for timeseries modelling. *Philosophical Transactions of the Royal Society (Part A)*. 41

[18] S. Ambikasaran, D. Foreman-Mackey, L. Greengard, D. W. Hogg, and M. O'Neil. Fast Direct Methods for Gaussian Processes. March 2014. 41

[19] L. E. DeWarf, K. M. Datin, and E. F. Guinan. X-ray, fuv, and uv observations of alpha centauri b: Determination of long-term magnetic activity cycle and rotation period. *The Astrophysical Journal*, 722(1):343, 2010. 41